

**UNIVERSIDAD DE INVESTIGACIÓN DE TECNOLOGÍA
EXPERIMENTAL YACHAY**

Escuela de Ciencias Físicas y Nanotecnología

**TÍTULO: STUDY ON THE POROSITY OF HOMOGENEOUSLY
DISPERSED CLAY/CARBON NANOTUBES
NANOCOMPOSITES**

Trabajo de integración curricular presentado como requisito para la
obtención del título de Físico

Autor:

Lajones Zapata David Eliseo

Tutor:

Dr. rer. nat. – Chacón Torres Julio César

Urcuquí, agosto del 2019

Urcuquí, 28 de agosto de 2019

SECRETARÍA GENERAL
(Vicerrectorado Académico/Cancillería)
ESCUELA DE CIENCIAS FÍSICAS Y NANOTECNOLOGÍA
CARRERA DE FÍSICA
ACTA DE DEFENSA No. UITEY-PHY-2019-00020-AD

En la ciudad de San Miguel de Urcuquí, Provincia de Imbabura, a los 28 días del mes de agosto de 2019, a las 14:00 horas, en el Aula Sala Capitular de la Universidad de Investigación de Tecnología Experimental Yachay y ante el Tribunal Calificador, integrado por los docentes:

<u>Presidente Tribunal de Defensa</u>	<u>Dr. PINTO ESPARZA, HENRY PAUL , Ph.D.</u>
<u>Miembro No Tutor</u>	<u>Dra. GONZALEZ VASQUEZ, GEMA , Ph.D.</u>
<u>Tutor</u>	<u>Dr. CHACON TORRES, JULIO CESAR , Ph.D.</u>

Se presenta el(la) señor(ita) estudiante LAJONES ZAPATA, DAVID ELISEO, con cédula de identidad No. 0951246156, de la ESCUELA DE CIENCIAS FÍSICAS Y NANOTECNOLOGÍA, de la Carrera de FÍSICA, aprobada por el Consejo de Educación Superior (CES), mediante Resolución RPC-SO-39-No.456-2014, con el objeto de rendir la sustentación de su trabajo de titulación denominado: Study on the porosity of homogeneously dispersed clay/carbon nanotubes nanocomposites, previa a la obtención del título de FÍSICO/A.

El citado trabajo de titulación, fue debidamente aprobado por el(los) docente(s):

<u>Tutor</u>	<u>Dr. CHACON TORRES, JULIO CESAR , Ph.D.</u>
--------------	---

Y recibió las observaciones de los otros miembros del Tribunal Calificador, las mismas que han sido incorporadas por el(la) estudiante.

Previamente cumplidos los requisitos legales y reglamentarios, el trabajo de titulación fue sustentado por el(la) estudiante y examinado por los miembros del Tribunal Calificador. Escuchada la sustentación del trabajo de titulación, que integró la exposición de el(la) estudiante sobre el contenido de la misma y las preguntas formuladas por los miembros del Tribunal, se califica la sustentación del trabajo de titulación con las siguientes calificaciones:

Tipo	Docente	Calificación
Presidente Tribunal De Defensa	Dr. PINTO ESPARZA, HENRY PAUL , Ph.D.	9,0
Tutor	Dr. CHACON TORRES, JULIO CESAR , Ph.D.	8,8
Miembro Tribunal De Defensa	Dra. GONZALEZ VASQUEZ, GEMA , Ph.D.	9,3

Lo que da un promedio de: 9 (Nueve punto Cero), sobre 10 (diez), equivalente a: **APROBADO**

Para constancia de lo actuado, firman los miembros del Tribunal Calificador, el/la estudiante y el/la secretario ad-hoc.


LAJONES ZAPATA, DAVID ELISEO
Estudiante


Dr. PINTO ESPARZA, HENRY PAUL , Ph.D.
Presidente Tribunal de Defensa


Dr. CHACON TORRES, JULIO CESAR , Ph.D.
Tutor



Dra. GONZALEZ VASQUEZ, GEMA , Ph.D.
Miembro No Tutor

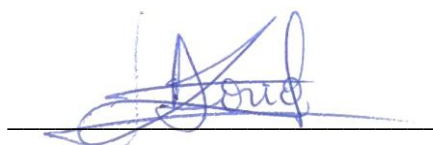


CIFUENTES TAFOR, EVELYN CAROLINA
Secretario Ad-hoc

AUTORÍA

Yo, **David Eliseo Lajones Zapata**, con cédula de identidad **0951246156**, declaro que las ideas, juicios, valoraciones, interpretaciones, consultas bibliográficas, definiciones y conceptualizaciones expuestas en el presente trabajo; así cómo, los procedimientos y herramientas utilizadas en la investigación, son de absoluta responsabilidad del autor del trabajo de integración curricular. Así mismo, me acojo a los reglamentos internos de la Universidad de Investigación de Tecnología Experimental Yachay.

Urcuquí, agosto del 2019.



David Eliseo Lajones Zapata

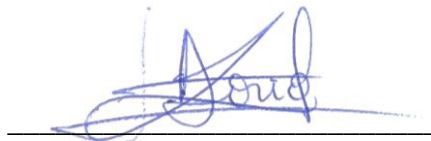
CI: 0951246156

AUTORIZACIÓN DE PUBLICACIÓN

Yo, **David Eliseo Lajones Zapata**, con cédula de identidad **0951246156**, cedo a la Universidad de Tecnología Experimental Yachay, los derechos de publicación de la presente obra, sin que deba haber un reconocimiento económico por este concepto. Declaro además que el texto del presente trabajo de titulación no podrá ser cedido a ninguna empresa editorial para su publicación u otros fines, sin contar previamente con la autorización escrita de la Universidad.

Asimismo, autorizo a la Universidad que realice la digitalización y publicación de este trabajo de integración curricular en el repositorio virtual, de conformidad a lo dispuesto en el Art. 144 de la Ley Orgánica de Educación Superior

Urcuquí, agosto del 2019.



David Eliseo Lajones Zapata

CI: 0951246156

Dedicatoria

Dedicado a mis padres Remigio Lajones y Carmen Zapata; su amor y sacrificios son lo que me ha llevado hasta dónde estoy ahora.

David Eliseo Lajones Zapata

Agradecimiento

Estoy muy agradecido con mi tutor, Dr. Julio Chacón, quien me ha ayudado a desarrollar este trabajo y cuyas palabras de consejo y apoyo estaban siempre listas cuando se necesitaban. He aprendido mucho sobre comunicación científica de él. Sus revisiones, comentarios y correcciones durante mi trabajo son muy apreciadas. Me gustaría también agradecer a mi co-tutora, Dr. Yadira Vega por las importantes conversaciones que tuvimos acerca de mi proyecto mientras realizaba mis pasantías bajo su tutela en el Instituto Tecnológico y de Estudios Superiores de Monterrey (ITESM). Esas pasantías me ayudaron mucho a comprender el comportamiento de los materiales que luego usaría para mi proyecto. También, agradezco el apoyo que me brindó el ITESM en forma de alojamiento y acceso a sus laboratorios durante mis pasantías. Doy gracias también a la Escuela de Ciencias de la Tierra, Energía y Medio Ambiente de Yachay Tech por el acceso a su equipo de nanotomografía para caracterizar mis muestras. En particular quiero agradecer a la técnica de laboratorio, Elizabeth Mariño, por su ayuda al operar el mencionado equipo. Un reconocimiento especial va dirigido a Dr. Juan Lobos quien ha sido una gran inspiración para mí desde mis primeros años en la universidad. El haberlo conocido es una de las principales razones por las que decidí estudiar física. No sería honesto de mi parte no mencionar a mis muy buenos amigos que han estado ahí en las buenas y malas: Claudia, Magno, Pablo, Charlotte, Diana, Mariana y muchos otros que he tenido el gusto de conocer. No hay agradecimiento suficiente que pueda dirigir a mi familia. Mi padre, Remigio Lajones; mi madre, Carmen Zapata; y mis hermanos; fueron todos, de una manera u otra un increíble apoyo para mí durante estos años. Ellos han tenido que sufrir mi ausencia en casa incluso en ocasiones importantes, pero aun así siempre han apoyado mi deseo y me han empujado a seguir mis sueños. Sin su inspiración y apoyo nada hubiera sido posible. Finalmente, quiero expresar mi agradecimiento a todos los científicos que me precedieron y cuyo trabajo en ciencia de materiales, electricidad, imágenes de rayos-x y geología me han facilitado y, de hecho, permitido realizar mi trabajo.

David Eliseo Lajones Zapata

Resumen

Los nanotubos de carbono (CNTs por su abreviación en inglés) son un material con propiedades electrónicas y mecánicas impresionantes. Se han convertido en un tema de investigación muy interesante. El diseño y fabricación de nanocompositos ha ido en aumento también para crear materiales con propiedades que se adapten a las necesidades de la industria. Los nanocompositos con CNTs muestran propiedades excelentes y son aplicados en áreas como óptica, electrónica, construcción y sanidad. En este trabajo presento un estudio sobre la porosidad de un compuesto de CNTs dispersados en una matriz de arcilla. Se usó dos tipos de arcilla: bentonita y caolinita. Los CNTs que se usó eran multi-capas. La porosidad del material se midió usando nanotomografía de rayos-x. Los resultados de este análisis son presentados, así como la relación obtenida entre el porcentaje de porosidad de las muestras y la concentración de CNTs. Los resultados indican reducciones de porosidad en ambos tipos de arcilla para concentraciones de CNTs de 0.01 y 0.05 % en peso; con una reducción mayor en la arcilla bentonita. El diferente grado de reducción de porosidad es atribuido a la estructura de las arcillas.

Palabras Clave:

Porosidad, Nanotomografía, bentonita, caolinita.

Abstract

Carbon nanotubes are a material with remarkable electrical and mechanical properties. They have become a highly important topic of research. Nanocomposite design and manufacture also has been on the rise as a means for creating materials with properties tailored to industrial needs. Nanocomposites added with Carbon nanotubes (CNTs) show excellent properties applied in areas as optics, electronics, construction and sanitation. Here we present a study on CNTs dispersed inside a clay matrix. Two types of clay were used: bentonite and kaolinite. The CNTs were multi-walled ones. The material's porosity was then studied using 3D X-ray Nanotomography. Finally, the results of this analysis are presented and a relationship between the concentration of CNT in the clay and the change in porosity is obtained. The results indicate relevant reductions of porosity in both types of clay for CNT concentrations of 0.01 and 0.05 wt. %. with a much higher reduction for the bentonite clay. The difference in reductions is attributed to the structures of the clays.

Palabras Clave:

Porosity, Nanotomography, Bentonite, Kaolinite.

Contents

1	Introduction	1
1.1	Introductory statement	1
1.2	Clay	2
1.2.1	Clay mineral	2
1.2.2	Clay structure	2
1.2.3	Clay properties	3
1.2.4	Electrical Properties of clay	4
1.3	Carbon allotropes	5
1.4	Carbon nanotubes	7
1.4.1	Types of carbon nanotubes	7
1.4.2	Properties of CNTs	8
1.5	Nanocomposites	10
1.5.1	Overview	10
1.5.2	Types of nanocomposites	11
1.5.3	Nanocomposite preparation methods	12
1.6	Porosity	13
1.6.1	Types of porosity	14
1.6.2	Pore volume measurement	14
1.6.3	Nanotomography	16
2	Motivation	17
2.1	Objectives	17

3	Characterization Method	19
3.1	X-ray Nanotomography	19
3.2	X-ray Nanotomography setup	22
4	Experimental Part	25
4.1	Preparation method	25
4.1.1	Mixture	25
4.1.2	Drying and moulding	26
4.2	Reconstruction of the samples	29
4.2.1	NRecon software	29
4.2.2	CTvox Software	30
4.2.3	CTAn software	31
5	Results & Discussion	33
5.1	3D reconstruction of the pristine Clay samples	33
5.2	3D reconstruction of CNT-Clay samples	34
5.2.1	Kaoln samples	35
5.2.2	Bentonite samples	36
5.3	Porosity analysis of the Kaolin group of samples	37
5.3.1	Plots of the porosity	37
5.4	Porosity analysis of the bentonite group of samples	37
6	Conclusions & Outlook	40
A	Complete Morphometry Results of the samples	42
	Bibliography	51

Chapter 1

Introduction

1.1 Introductory statement

Nanocomposites are materials that have been modified at the nano-level.¹ Due to the interactions between the constituents, unique properties are shown by the nanocomposites.² The study of the properties and benefits of nanocomposites are some of the most important areas of study.³ Knowing not only what properties can be obtained from certain combination, but also how those arise is crucial for the improvement of manufacturing techniques and finding new applications for these materials. In this work I will characterize two types of clays functionalized with carbon nanotubes using x-ray nanotomography technology. The study will focus in the analysis of the porosity using nanotomography imagery and a software for image analysis. In the introduction chapter, I will describe the materials involved in the creation of the nanocomposite of interest: clay minerals and multi-walled carbon nanotubes. Also, a brief history of the nanotubes and clays used for this project, together with their individual properties, and how they are currently used in industry will be provided. Then, I will introduce some common manufacturing techniques for the creation of nanocomposites; following, the motivation chapter will expose the importance of this project. In the characterization chapter I will present the technology and physics behind the working principle of a nanotomography equipment. Then, I will discuss about the specific setup and lab conditions used for the measurements discussed in the results chapter. The results and discussion section will include images as well as tables and plots of the obtained data and their corresponding discussion. Finally, in the conclusions and outlook chapter, a concluding

statement about the results will be made. For the outlook part, possible flaws in the accuracy and certainty of the results will be presented together with ways to improve them and possible subsequent work in the area.

1.2 Clay

The term clay refers to certain types of naturally occurring materials that are composed primarily of fine-size minerals, show plastic behavior at the correct water absorption level, and will harden when deprived of water by drying or cooking.⁴ It must not be confused with the term "clay mineral", described below, as it refers to the actual minerals found inside clay soil.⁵ The definitive grain size of clay varies between disciplines from $<1 \mu\text{m}$ to $<4 \mu\text{m}$. The use of the upper limit is suggested by Weaver⁴. The most commonly used clays in industry are: Bentonite whose main clay mineral constituent is montmorillonite; kaolins composed mainly of kaolinite, palygorskite and sepiolite; and "common clays" which are often composed of illite-smectite minerals and are mostly used in ceramic fabrication.⁴

1.2.1 Clay mineral

Clay minerals are defined by the Joint Nomenclature Comitees (JNC) of the Association Internationale pour l'Etude des Argiles (AIPEA) as hydrous phyllosilicates that cause plasticity of clay and which upon drying or firing, will harden.⁵ Since the definition does not include the origin of the mineral, synthetically manufactured materials also fall in that definition. Also, the failure to assert a certain grain size limit, allows for phyllosilicates of any size to fall in this group.⁶ The term "clay mineral" must not be confused with "clay" as the latter can describe a rock, sedimentary deposit, and the residues of the alteration of the former.⁷

1.2.2 Clay structure

The structure of clay is just the accumulation and intercalation of clay mineral platelets. Based on their stratification, the phyllosilicates platelets, can be classified as 2:1 or 1:1. The format "a:b" refers to the ratio of tetrahedral silicates to octahedral hydroxide layers in a single sandwich-shaped clay platelet; the "a" index represents the number of tetrahedral layers, and the "b" index

represents the number of octahedral layers. Consequently, a 2:1 clay consists of two Silicate layers sandwiching an octahedral Aluminium hydroxide layer (see Figure 1.1 *a*), and a 1:1 clay consists of one tetrahedral silicate layer and one octahedral Aluminium hydroxide octahedral layer (see Figure 1.1 *b*).^{6,7} These platelets, depending on their internal structure can attract cations and water to its surface. This is how some clays swell when wet and others do not. Additionally these interlayer materials modify the charge of the platelets. See Table 1.1 for examples of the different types of clays based on their structure.⁷ Kaolin and Bentonite are composed respectively of Kaolinite and montmorillonite. The former belongs to the group of serpentine-kaolin and is found without additive or only water on its surface. Meanwhile, the later belongs to the smectite group and is commonly found hydrated and with cations on its surface.⁷

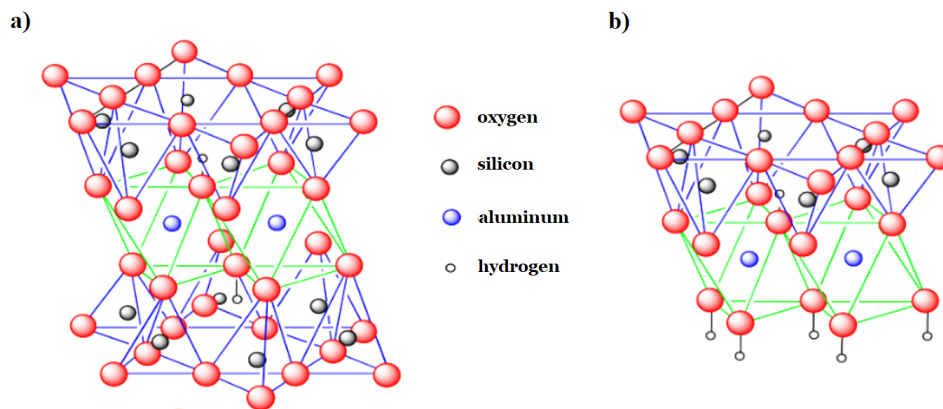


Figure 1.1: Crystalline structure of clay minerals. *a*) 2:1 tetrahedral-octahedral-tetrahedral structure, *b*) 1:1 tetrahedral-octahedral structure. Adapted from Schaller⁸.

1.2.3 Clay properties

Clays can exhibit remarkable properties. First, by definition they swell when wet and will harden when dried or fired. The Food and Drugs Administration gives them the GRAS classification, which means it is safe for use in food and medicine.⁹ In mechanical properties, there have been measurements of the Young's modulus along the tubes axis of up to 180 GPa.⁹ Young's modulus measures the ability of a material to withstand changes in length when tension or compression

are applied lengthwise. For comparison, the Young's modulus of steel is between 186 and 214 GPa.¹⁰ It also offers a effective surface area of up to 750 m²/g,⁹ which boosts its adsorption capabilities to be used as a catalyst and the storage of gasses. Also, one dimension of its layered structure in the manometer scale; the 1:1 layer has a thickness of around 0.7nm , while the 2:1 has one of around 1 nm.⁶ This is mostly useful when they are going to be mixed with nano-scaled materials such as carbon nanotubes.

1.2.4 Electrical Properties of clay

Depending on how the ions are replaced inside the octahedral or tetrahedral sheets inside the tetrahedral-octahedral-tetrahedral(TOT) or tetrahedral-octahedral (TO) layer (see Figure 1.1), the corresponding layer can stay neutral or become positively or negatively charged.¹¹ Electrical neutrality exist if either the octahedral layer or the tetrahedral layer is neutral. The tetrahedral layer remains neutral if there are Si⁴⁺ in all the tetrahedral sites.¹² On the other hand, the octahedral layer offers more flexibility and can be neutral if one of two scenarios occur: (i) if there are trivalent cations (Al³⁺ and/or Fe³⁺) in two of the octahedral sites while the third is left vacant [(Al/Fe)₂³⁺ (OH)₆], (ii) if there are divalent cations (Fe²⁺, Mg²⁺, Mn²⁺) in all three octahedral sites [(Fe/Mg/Mn)₃²⁺ (OH)₆].¹² Electrical Neutrality is broken when: (i) Si⁴⁺ is substituted by Al³⁺ in tetrahedral sites, resulting in a -1 charge per substitution; (ii) Mg²⁺ is substituted by Al³⁺, resulting in a +1 charge per substitution; or (iii) total vacancies in the tri-octahedral sheet, resulting in a -6 charge per tri-octahedral vacancy.^{12,13}

Interlayer material	Group	Example Species
1:1 Clay minerals		
None or H_2O	Serpentine-Kaolin	Amesite, fraipontite, odinite, dicktite and Kaolinite
2:1 Clay minerals		
None	Talc-pyrophyllite	Kerolite, pimelite, talc and pyrophyllite
Hydrated cations	Smectite	Hectorite, Montmorillonite, volkonskoite, saponite and montronite
	Vermiculite	Tri-, di-octahedral vermiculite
Non-hydrated cations	True (flexible) mica	biotite, lepidolite, celadonite, muscovite, illite and glauconite
	Brittle mica	Anandite, bityite, margarite and kinoshotalite
Hydroxide sheet	Chlorite	Baileychlore, clinochlore, nimate, donbassite, cookeite, etc.
Regularly interstratified 2:1 clay minerals		
		Aliettite, corrensite, kulkeite, rectorite and tusodite

Table 1.1: Examples of Hydrous Phyllosilicates divided in groups based on their interlayer additives. Adapted from Martin *et al.*⁷.

1.3 Carbon allotropes

Carbon atoms are very important in human life and research. Every living being is formed down to the molecular level by carbon-including molecules.¹⁴ Additionally hydrocarbons power most of our vehicles, industries and electricity generation.¹⁵ One of the reasons for carbon's versatility is the high capability that it has to bond with other atoms.¹⁶ It can form one, two, three, or four covalent bonds, and the quantity of molecules containing carbon is astonishingly high.¹⁷

When carbon bonds to other carbon atoms, very different structures may arise depending on how many carbon atoms it is connected to. Diamond is a naturally occurring material where each carbon is bonded to other 4 carbons in an sp^3 hybridisation.¹⁶ Hence, diamond is such a good

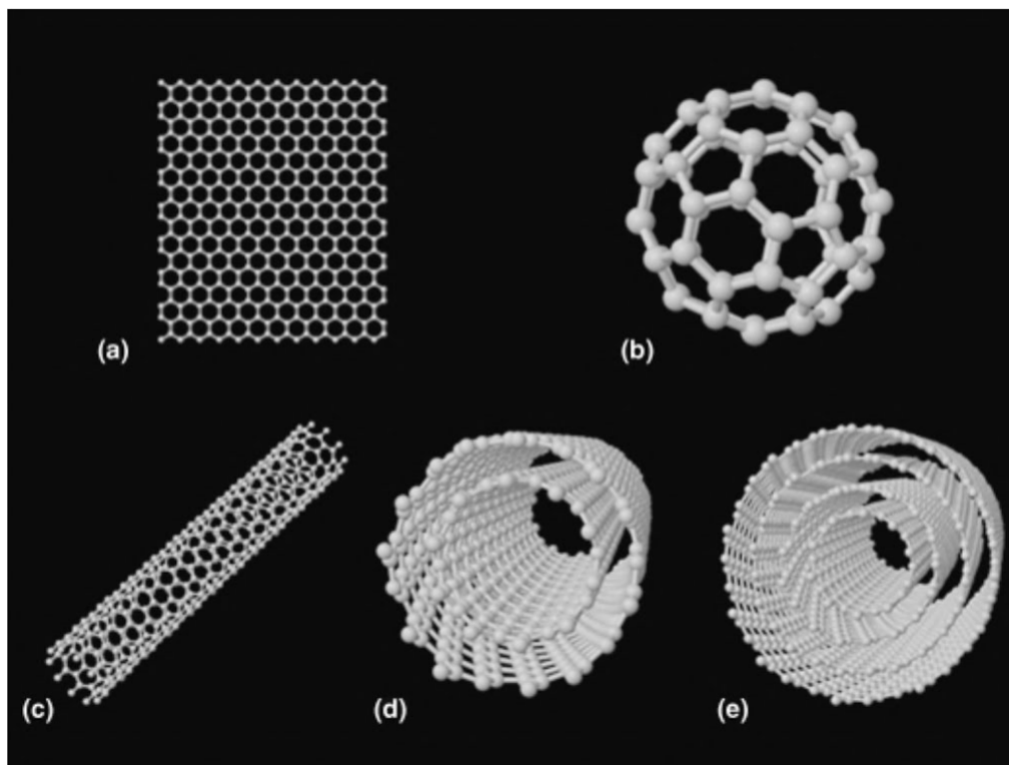


Figure 1.2: Different sp^2 carbon configurations. (a) graphene layer; (b) C_{60} fullerene; (c) SWCNT; (d) DWCNT; (e) MWCNT. Adapted from Grady¹⁷.

insulator because all carbon electrons are involved in a covalent chemical bond and no electron is free to conduct electricity. On the other hand, in graphene (Figure 1.2 a) and some other fullerenes (Figure 1.2 b-e), carbon is found bonded just to 3 other carbon atoms in an sp^2 hybridisation.¹⁸ This leaves an extra electron that can act as a charge carrier, and thus these materials can conduct electricity. Graphene sheets are planar while fullerenes show curvature.¹⁷

Fullerenes can be divided in two major groups: buckyballs (Figure 1.2 b) and carbon nanotubes (Figure 1.2 c-e). Fullerenes are composed of sp^2 carbon atoms that have been arranged in an spheroidal or tubular structure, for buckyballs and carbon nanotubes (CNTs) respectively.¹⁶ The work on this materials started in 1986 with the discovery of buckyballs by Rick Smalley, Robert Curl, and Harry Kroto, whom were awarded the Nobel Prize in Chemistry for this discovery 10 years later in 1996.¹⁹ Even though their discovery yielded a Nobel Prize, there are very few

industrial applications that make use of or are based on buckyballs.¹⁸ On the other hand, their tubular counterparts, CNTs, have found a lot of interest in the scientific community for their staggering properties.²⁰

1.4 Carbon nanotubes

Carbon nanotubes (CNTs) are cylindrical allotropes made of carbon atoms. In CNTs carbon atoms are interconnected in a closed hexagonal mesh with radius ranging from 0.4 to 100 nm²¹. These nanostructures show extraordinary properties like high stiffness and high electric conductivity that make them of great importance for fields such as optics, electronics, and nanotechnology²⁰.

1.4.1 Types of carbon nanotubes

Carbon nanotubes can first be classified with respect to their amount of concentric tubes. A single-walled carbon nanotube (SWCNT) consists of one tube (Figure 1.2 *c*), a double-walled carbon nanotube (DWCNT) consists of two (Figure 1.2 *d*), and a multi-walled carbon nanotube (MWCNT) consists of more than two concentric tubes (Figure 1.2 *e*).¹⁸ In a single-walled carbon nanotube, the manner in which the graphene layer is rolled will determine the chirality of the nanotube (see Figure 1.3 *a*).²⁰

From the infinite linear combinations of a_1 and a_2 vectors, two special chiralities can be recognised: $n=m$ and $m=0$; the former one is named armchair configuration and the later is named zigzag configuration.²¹ Their names are based in the edges of the respective tubes, c) and b), in Figure 1.3. These configuration are not chiral, *i.e.* they do not have an enantiomeric pair. The diameter d of a single-walled carbon nanotube can be extrapolated from its n,m parameters using the next formula:

$$d = \frac{a_{C-C} \sqrt{3(n^2 + mn + m^2)}}{\pi} \quad (1.1)$$

where a_{C-C} is the length of the carbon-carbon bond (1.42 Å).

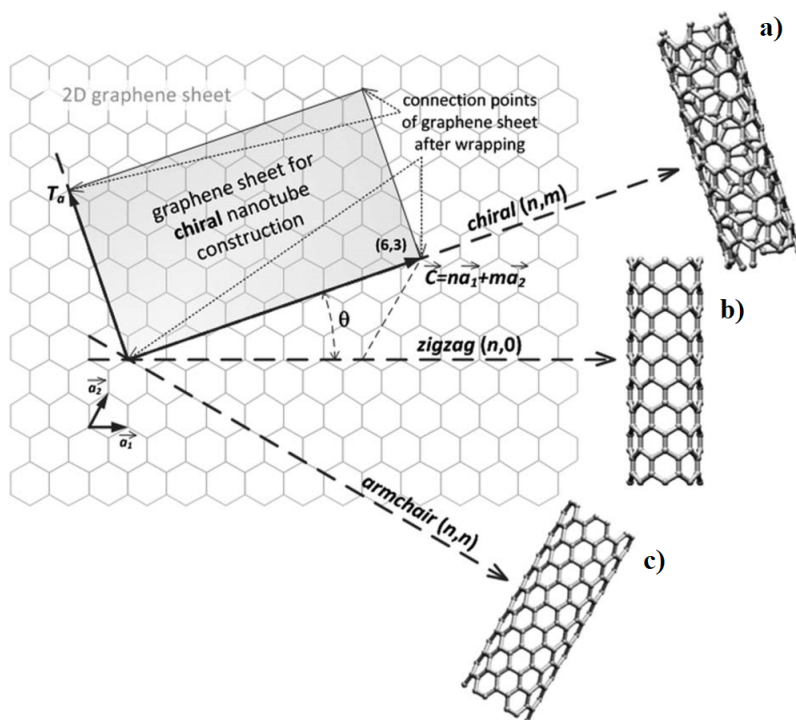


Figure 1.3: Schematic on the different nanotube structures depending on its (n,m) parameters. T_0 is the axis along the tube; a_1 and a_2 are the lattice vectors of graphene; C denotes the direction in which the nanotube rolls. $c)$ $n=m$ configuration; $b)$ $m=0$ configuration; $a)$ arbitrary n & m configuration. Modified from Sanginario *et al.*²²

1.4.2 Properties of CNTs

As it was mentioned before in this section, carbon nanotubes exhibit some extraordinary properties that are the main reason of the high interest the industry and the scientific community have on them.²⁰ However, measuring these properties is not often an easy task. The small size of the nanotubes makes it almost impossible to perform measurements in an individual nanotube.²¹ On the other hand, the fact that a batch of nanotubes can include several different types of CNTs makes their analysis more complex.²⁰ Most of the properties predicted for carbon nanotubes are first theoretically proposed based on a study of their chemical bonding environment. Great efforts are being made by experimentalists to obtain measurements of those properties. In the

following sections, a revision of these properties will be made and, when available, experimental measurements will be commented as well.²¹

Mechanical properties

In terms of tensile strength and elastic modulus, carbon nanotubes are the strongest material discovered till now.¹⁰ In Table 1.2 are depicted the experimental and theoretical data of the mechanical properties such as Young's modulus, tensile strength and elongation at break of different types of nanotubes. There was also included data for stainless steel and kevlar for comparison. The experimental section of the chart shows already the superiority of CNTs over steel and kevlar. Moreover, the theoretically predicted values are even higher than those experimentally measured.²³ However strong along their axis, nanotubes have been found to be rather soft in the radial direction²⁴. This can be attributed to their hollow interior and the fact that, in single-walled carbon nanotubes, the circle section offers no resistance to deformation, and that in multi-walled carbon nanotubes, there is no covalent bond between their concentric layers to offer support in the radial direction.^{10,24}

Material	Young's modulus (TPa)	Tensile strength (GPa)	Elongation at break (%)
Theoretical			
Armchair SWCNT	0.94	126.2	23.1
Zigzag SWCNT	0.94	94.5	15.6-17.5
Chiral SWCNT	0.92		
Experimental			
SWCNT	≈ 1	13-53	16
MWCNT	0.2-0.8-0.95	11-63-150	
Stainless steel	0.186-0.214	0.38-1.55	15-50
Kevlar 29&149	0.06-0.18	3.6-3.8	≈ 2

Table 1.2: Comparison of Mechanical Properties between different types of CNTs. The chart shows the values for Young's modulus, tensile strength and elongation percentage at breaking

point. The data is divided into theoretically predicted values and experimentally measured ones. For any empty cell it should be assumed that the value has not been calculated and/or measured. Created using data from Yu *et al.*¹⁰, Grady¹⁷, Nan²¹, Yu *et al.*²³, Ruoff *et al.*²⁴.

Electronic properties

The unique electrical properties of CNTs arise mainly from their sp^2 hybridisation. This configuration leaves one electron free and above the CNT's surface.²⁵ This means that there can be electric conductivity along the nanotube axis but not perpendicular to it. The conduction and valence band depend highly on the standing waves that go around the nanotube. Theoretical calculations performed on nanoribbons "unzipped tubes" show that once the tubes are flattened, the electrical behaviour depends solely on the n, m parameters. Metallic conduction occurs when $n - m = 3q$, where q is an integer. Thus, all armchair nanotubes are metallic, and from the rest; $2/3$ behave as semiconductors, and $1/3$ behave as conductors.²⁶ In a metallic nanotube, there is an almost linear relation between current and voltage starting at 0 V. A semi conducting nanotube will not conduct any electrons until a threshold voltage is surpassed; this is needed to overcome their energy band-gap. After that, a linear relation between current and voltage as that of the metallic nanotubes appears. However, at room temperatures the gap is so small that these tubes are effectively considered as metallic. Finally, bundling metallic nanotubes will increase their band gap, turning them semiconducting but still with a small band gap in the order of 0.1 eV.²⁷

1.5 Nanocomposites

1.5.1 Overview

The term nanocomposite makes reference to a multi-phase solid material where the size of at least one of the constituent phases is between 10 to 100 nm. The idea of adding a nanostructure (filler) to a macroscopic material (matrix) dates back to 1950, when clays were used as flow control agents in polymer solutions such as paint²⁸. However, according to José-Yacamán *et al.*²⁹, humans had used nanostructured materials long before there was a physical understanding of them; in that work they reported that a pre-columbian pigment used in Mesoamerica, Maya blue, was in fact a nanostructured material.

The main interest in these materials is to obtain products with properties that surpass those the constituents would show by themselves. Examples of modified properties in materials are: magnetism, hardness, elasticity, hardness, refractive index, thermal and electrical conductivity, and mechanical strengthening.¹

1.5.2 Types of nanocomposites

Nanocomposites are mainly classified based on their matrix, and their construction.³⁰ Three main groups are denoted: polymer, ceramic, and metal matrix nanocomposites. The mechanics of the formation and the behavior of each type differs highly from one to another.²

Polymer Matrix Nanocomposites

Polymer nanocomposites are materials where the matrix is a polymer and nanostructures are added to it. Examples of polymer matrices include: thermoplastics, thermosets, elastomers, and natural and biodegradable polymers.³¹

Ceramic Matrix Nanocomposites

Ceramic nanocomposites are rapidly gaining interest in the industrial sector. The microstructure of these composites grants them outstanding mechanical and electrical properties.³¹ Some examples include: $\text{Al}_2\text{O}_3/\text{SiO}_2$, SiO_2/Ni , $\text{Al}_2\text{O}_3/\text{TiO}_2$ and $\text{Al}_2\text{O}_3/\text{CNT}$.

Metal Matrix Nanocomposites

Metal Nanocomposites consist of a metal or an alloy of metals where nanoparticles are introduced for reinforcement. The nanoparticles are often used to impart or improve wear resistance and mechanical properties in general. At the nano-level the addition of nanoparticles creates a barrier in dislocation movement, hence improving the mechanical properties. Some examples include: $\text{Fe-Cr}/\text{Al}_2\text{O}_3$, $\text{Ni}/\text{Al}_2\text{O}_3$, Al/CNT and Mg/CNT .²

1.5.3 Nanocomposite preparation methods

Many methods and combinations of those processes are devised to prepare different types of Nanocomposites; as explained in the following

Intercalation

In this method the nanomaterial is dispersed into the micro-scale matrix. It often requires a surface modification of the filler in order to make it more compatible with the matrix and assure an homogeneous dispersion. The nano-fillers can be dispersed using one of the following two techniques³²⁻³⁴:

- **Chemical approach:** This is mostly used in Polymer matrix nanocomposites.³³ In this process the nanoparticles are first dispersed in a monomer and later the polymerization occurs; the nano-fillers are swollen with monomer solution and then the polymer forms around the nano-fillers.
- **Mechanical approach:** In this process simple mechanical mixing is used to distribute the single nano-fillers inside the matrix.² Generally, before mixing, both the nano-fillers and the matrix component are dispersed in a common solvent; then, the two solutions are mixed. The solvent is then dried off the nanocomposite.

Melt intercalation

This method is rapidly gaining terrain in the industry for the easiness with which it adapts to production line processes in factories. In this method, the nano-fillers and the matrix components are mixed at molten temperatures. Thus, the method is compatible with extrusion and ejection molding. It also allows nano-modification of polymers that are not suitable for in-situ polymerization or solution intercalation.^{31,35}

***In-situ* polymerization**

In this method the nano-fillers are swollen in monomer solution. The monomer easily leaks through the nano-fillers assuring dispersion. Then, the material is polymerized using radiation, heat or initiator-polymerization depending on the polymer.^{32,34}

Sol-Gel method

This is a bottom up approach opposite to those methods previously described. The term sol-gel comes from the two steps in the process: sol and gel. Sol is a suspension of the nanoparticles in a monomer solution and gel refers to the interconnected mesh between phases once the polymerization has occurred. Here the polymer serves as nucleation sites for crystal layers to grow. As the crystals form, the polymer seeps through the layer and the nanocomposite is formed.³⁴

Direct mixing

This is a top-down approach consisting in the breakdown of the nanofillers during mixing process. This method is most applied to make polymer matrix nanocomposites.^{34,35} There are two ways of mixing the polymer with the nanofillers:

- **Melt compounding**; here the nanofillers are added to the polymer above the glass transition temperature of the later. Here the force braking down the nanofillers is mainly the viscous drag caused by the polymer movement. This viscous drag also causes the nanofillers to disperse homogeneously inside the polymer.³⁵
- **Solvent method**; in this method, nanoparticles and the polymer are dissolved in a co-solvent. Once the materials have been mixed, the solvent is evaporated. In this method there is not much shear stress introduced in the matrix as in the melt compounding method and the nanofillers have to be pre-dispersed in the solvent via sonication.³⁴

The nanocomposites resulting of the methods above are then processed by conventional fabrication methods such as casting, compression and injection molding, extrusion, etc.^{2,31,33,34}

1.6 Porosity

Porosity is the quantification of the amount of empty space inside a solid material.³⁶ These empty spaces are called pores. Pores can be connected and disconnected: Connected pores are those that are in contact with another pore and so ensure fluid flow between them, disconnected pores

are those that are separated by solid material from other pores and so fluid can not flow into or out of them.³⁷ Porosity is often associated with different quantities describing the pores:

- **Pore surface;** It is a measure of the sum of the area surrounding the pores and is often measured only for the connected pores.³⁸ It is highly important for characterizing the effectiveness of porous media destined for catalysis since the speed-up of the process depends highly in the amount of catalytic surface available.³⁹
- **Pore size distribution;** It is a measure of how many pores fall in certain size range.^{36,40} It determines the homogeneousness of the pores and has implications in how forces move through the material, which has implications in mechanical tests.⁴¹
- **Pore volume;** It is a ratio between the empty space caused by the pores and the entire volume the solid object occupies.³⁶ Aerogels, for example, have the largest pore volume ratio which in turn makes them the lightest artificial material.⁴²

In this work, porosity will refer to the measurement of pore volume.

1.6.1 Types of porosity

Depending on the connection between the pores inside a sample and with the exterior environment, the porosity can be classified as open and closed.³⁶ Open porosity is the name given to the pore space inside a material that is accessible from the outside and through which liquid or gas flow is possible.³⁸ It is also referred to as interconnected or effective porosity because this porosity can interact with exterior materials and also because only this type of porosity helps add to the effective surface area of the material.³⁹ Because of that, it can be directly measured with conventional methods (See section 1.6.2). Closed porosity is the name given to pore space that is not accessible from outside the bulk of the material.³⁷ This type of porosity is related to the impermeability and insulation capabilities of the material and it also helps reduce weight.^{43,44} The total porosity of a material is the sum of the both types.

1.6.2 Pore volume measurement

There are many ways for measuring pore volume inside a solid. Here I will introduce the most common:

Mercury Intrusion method

In this method, the sample which is to be characterized is put into a chamber partially filled with mercury and the rest with air at a known pressure (e.g. atmospheric pressure). Then a force is applied to the mercury and it is forced into the pores of the solid. Since the volume of mercury inside the chamber is known and it is due to change as it enters the solid, a good approximation of the connected pore's volume can be made.⁴⁵

Gas expansion method

This method is based on the Boyle-Mariotte gas Law. Boyle-Mariotte law says that at constant temperature and low pressure, the pressure and volume of an ideal gas are inversely proportional.⁴⁶ This is one of the most used methods for measuring pore volume. The set up varies but in general is composed of two chambers of known volumes, V_0 and V_1 . The sample is then placed inside the first chamber and said chamber is pumped up with gas to certain pressure P_0 . Then the other chamber, initially at pressure P_1 is connected to the first and the gas flows between them until equilibrium is reached.⁴⁷ Then the final pressure P_2 is measured and from Boyle-Mariotte law we have:

$$\frac{P_0(V_0 - V_S)}{Z(P_0)} + \frac{P_1 \times V_1}{Z(P_1)} = \frac{P_2(V_0 + V_1 + V_S)}{Z(P_2)} \quad (1.2)$$

where V_S is extracted as the volume of the solid. The difference between the total volume of the object and V_S gives the pore volume of the object. Helium is usually used as an approximation to an ideal gas at low pressure and Z is set to 1 according to the ideal gas assumption.⁴⁷

Computed tomography method

For this method an industrial CT device is used to scan the sample and generate a computer 3D model of it. Then an analysis of defects on the model is used to extract a 3D model of only the pores. From that last model, one can measure pore volume, pore size distribution, and pore surface. Moreover, this method allows for the measuring of those variables on connected pores as well as on disconnected ones.⁴⁸ In this work I will use this method to measure the porosity of my samples and a more detailed description of the method as well as the specific device used for this work can be found in Chapter 3, Characterization Method.

1.6.3 Use of nanotomography to measure porosity

Micro- and nanotomography have been used to study a wide range of rock, soils, and other systems. While its main use has been for imaging, a large quantity of studies regarding internal structure distribution,⁴⁹⁻⁵⁴ and specifically porosity, have been published. These studies not only focus on obtaining porosity values of the materials but also on the parameters of the setup. Energy of the x-ray beam,⁵⁵ size of the sample, distance to the source and detector,⁵⁶ attenuation values for thresholding of pores,⁵⁷ etc. have been studied as parameters that affect the accuracy of the porosity measurement of the material.

The work of Ostadi *et al.*⁵⁷ shows how threshold selection in the binary images to map the pores can influence greatly the results of further analyses, specifically, simulated flow through the 3D model of the system. In that work they studied the changes in flow behavior over increments of 0.4 % of the threshold value on the greyscale nanotomography scans of polymer electrolyte fuel cells. They found that the flow properties of the material are greatly affected by the selection of thresholding values. The work of Tkachuk *et al.*⁵⁵ describes the use of an 8 keV source to obtain scans of a solid oxide fuel cell with resolution down to 50 nm. These studies, between others, try to tackle two of the main issues with nanotomography porosity measurements: resolution and accuracy discerning between pores and bulk material exactly. These issues will affect the results presented in this work and will be taken into account within the discussion and analysis of the results.

Chapter 2

Motivation

In chapter 1, I discussed the unique properties that both clay and carbon nanotubes show. One important property of CNTs is their longitudinal strength which may enable them to hold the clay matrix together. These effects may result in the modulation of the porosity of the material by means of an increased resistance to the formation of pores. Thus, the interest in measuring the porosity of the different clay to CNT ratios arises. In order to measure the porosity we used x-ray nanotomography. This technique is known for its use in 3D reconstruction of the internal structure of materials and most specifically in retrieving data about pore size and distribution.⁵⁶ By analyzing the porosity percentage with respect to the bulk material in the different samples a relation between the CNT content and the changes of porosity will be stated.

2.1 Objectives

The research objectives that will be tackled in this thesis are as follows:

1. **Usage of 3D x-ray nanotomography as a technique for porosity measurement:** The measurement is done using BRUKER hardware and software for scans acquisition and image analysis. The pore structure data obtained is the pore volume.
2. **Quantitative comparison of pore volume between different added concentrations of CNTs added to clay as well as structural characteristics specific to each clay type:** This is done between the two clay types used and between groups belonging to the same clay

type. The porosity is plotted as a function of the concentration of CNTs in the samples and the structural characteristics are extracted visually from the 3D reconstructed models.

Chapter 3

Characterization Method

3.1 X-ray Nanotomography

X-rays were discovered back in 1895 by Dr. Wilhelm Röntgen. Röntgen was experimenting with metallic electrodes separated inside a vacuum chamber. When he applied high voltages to those plates a phosphorous material elsewhere in the lab would glow.⁵⁸ The reason for this glowing was the emission of high energy invisible electromagnetic radiation known as x-rays. When Röntgen placed his hand between the experiment and the glowing material he saw what seemed to be a projection of his hand in the glowing material. With further experimentation it became clear that x-rays could be used for imaging and medical diagnosis.⁵⁸ currently x-rays are used in a wide range of applications. In medicine, it is used to detect fractures and bone malformations.⁵⁹ It is also used in airport security to look inside people's luggage without opening it.⁶⁰ Art is another area where it is used; mainly to uncover counterfeit pieces painted over an existing one.⁶¹ They are also used for radiation therapy a treatment for cancer patients where x-ray is used to destroy tumours.⁶²

The core idea behind x-ray imaging is the fact that x-rays are absorbed at different levels by different materials depending mainly on their density. X-rays are high-energy photons.⁵⁹ When they traverse a material they crash with other particles. The more particles it has to interact with, the more energy the beam loses. Thus, the longer or denser the material the darker it will look in an x-ray image, while thin and/or low density materials will look brighter.⁶³ Tomography devices in general use this principle to create images of the inside of samples; being it of people in a

hospital using computerized axial tomography (CAT) devices, or, for solid samples in general, using a 3D x-ray nanotomography system.⁵⁶

In 3D x-ray nanotomography, x-rays from a source are focused onto the specimen to be studied and go through finally hitting a detector at the other side.⁵⁶ The sample rotates and another image is taken. The process repeats until the sample has rotated 360°. The images are used to reconstruct a stack of computer generated slices of the sample. These slices can be used to reconstruct a 3D render of the sample or to interpolate different data like pore size, connectivity, etc.⁶⁴ It thus appears as a great tool to characterizing the interior of nanocomposite samples without destroying the original.

There are two main types of x-ray nanotomography: synchrotron based and lab based. They differ primarily in the nature of the source. In synchrotron x-ray nanotomography, the x-rays are generated by charged particles accelerated inside a curved chamber using electromagnets. This configuration offers certain advantages as higher energy, higher flux and higher coherence of the beam which result in overall higher resolution of the acquired images (See Figure 3.1 *a*).⁵⁶ Lab x-ray nanotomography on the other hand produces inside an x-ray tube. An x-ray tube is an evacuated chamber inside which electron are accelerated at high voltage towards a metallic electrode. When they hit the electrode, the electron will knock inner shell electron from their orbitals. As the electrons fall down to occupy the space left, x-rays are emitted. These x-rays are then focused onto the sample (See Figure 3.1 *b*). This configuration offers the advantages of being less expensive, smaller and more convenient than their synchrotron counterparts as synchrotron time is highly demanded and often is only available for very short-lasting experiments.^{56,59}

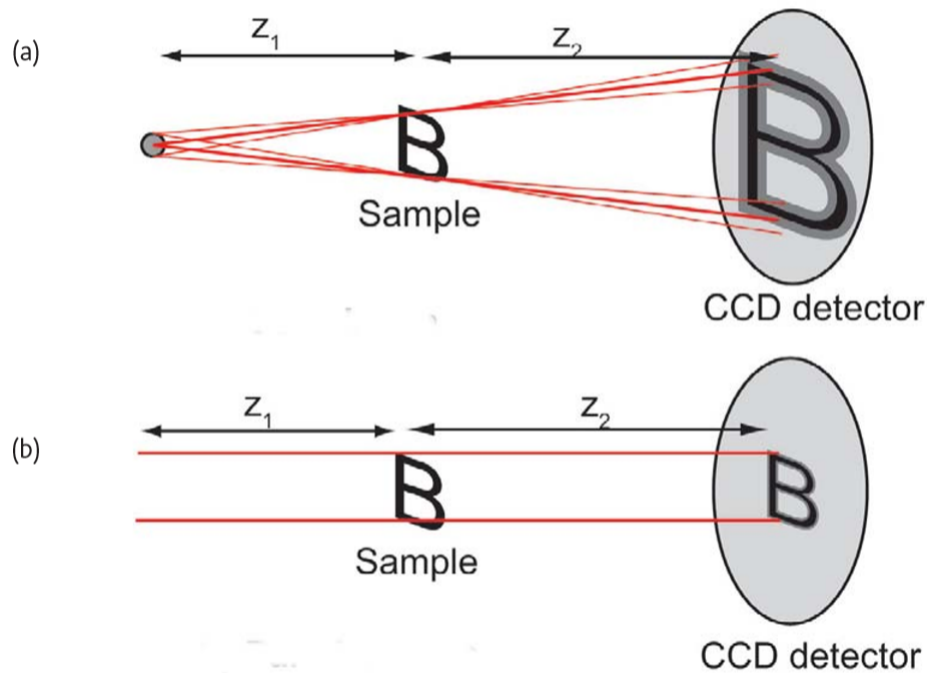


Figure 3.1: Depiction of the x-rays output of; (a), a lab based and, (b), a synchrotron based x-ray nanotomography imaging device. In (a), the source generates a cone beam to project an image of the sample in the detector. (b) shows the high coherent beam generated in a synchrotron as the source is very far from the sample. Z_1 and Z_2 are the distance from the source to the sample and from the sample to the detector respectively. In *a*, as Z_1 decreases compared to Z_2 , the beam becomes incoherent resulting in a blurry image. In *b*, Z_1 is so big it is considered inf resulting in a clearer image. Adapted from Withers⁵⁶.

In general, samples do not require preparation to be placed inside the nanotomography device.⁶⁴ However, certain points must be considered: First, the samples cannot be liquid; if the particles inside the sample are moving, the resulting images may not represent the original sample at all. Second, while the shape does not matter, having a cylindrical symmetry helps with positioning the sample at the right distance from the source and avoiding collisions between the sample and the source. Finally, as the field of view of the source is constant, a big sample will be placed further from the source and thus the pixel size will be bigger, resulting in lower resolution.⁵⁶

The smaller the features one tries to resolve in the detector, the smaller the sample should be. Once that is sorted out, the sample does not require further preparation like pulverization, fine slicing, grinding or sputtering.⁶⁴ This is an advantage over other measurement techniques that require highly skilled users both for the usage and the preparation of the sample.

This chapter covers the setup in which and how the samples were measured. Here are included a description of the the x-ray nanotomography equipment used, together with important data for the reproducibility of this work.

3.2 X-ray Nanotomography setup*

The nanotomography equipment used was a lab based Bruker SkyScan 2211. This apparatus is able to hold samples of up to 300 mm in diameter and 400 mm in height. The positioning system consists of a piezoelectric system with an error below 50nm in any axes and it is mounted over an anti-vibration granite table; these two features help to stabilise the sample and to avoid aberration in the images caused by unwanted movement of the sample (see Figure 3.2). The lowest rotation step is of 0.1°/step, this helps to get very detailed scans of the samples as long as time is not limited. The x-ray source is an X-ray Worx XWT-240-CT with a tungsten target. This specific setup allows for voltages between 20 and 240 kVolts and currents between 0.05 and 0.3 Amps with a maximum power output of 300 Watts. This device was equipped with two detectors: The 6 Mp flat-panel for big objects which has a lower resolution and an 11 Mp cooled CCD with wide field of view for higher spatial resolution. It offers also the capability of applying filters to the source. Filters here consist on pieces of different metals each wit higher atomic number. The work of the filters is to stop photons with energies below certain threshold to hit the sample. The device offered the possibility to mount an Al filter of 0.5 mm thickness.

The samples measured for this work were scanned at a source current of 75 kV and a source current of 180 uA. They were scanned using the micro-focus mode and the images were acquired

*I was present during every step of the operation of the SkyScan equipment nanotomography setup and I decided which parameters were used for the different features of the setup. The SkyScan was directly handled only by the Laboratory technician in charge, Elizabeth Mariño, based on internal regulation from the university. In Ecuador, a license is required for operating radioactive capable equipment such as the one used here, and I lacked of this license and only oversaw the image acquisition part of this work. This is the only step of the work when I outsourced a task to other person, prior and afterwards all the work project was done by myself.

using the flat-panel detector. The acquisition time per image was set to 95 *ms* with the pixel size set to 9.0 μm . The filter assembly was closed and the Al filter was used. The rotation step was set to 0.2°. The frame averaging function was on and 3 frames were averaged per image.

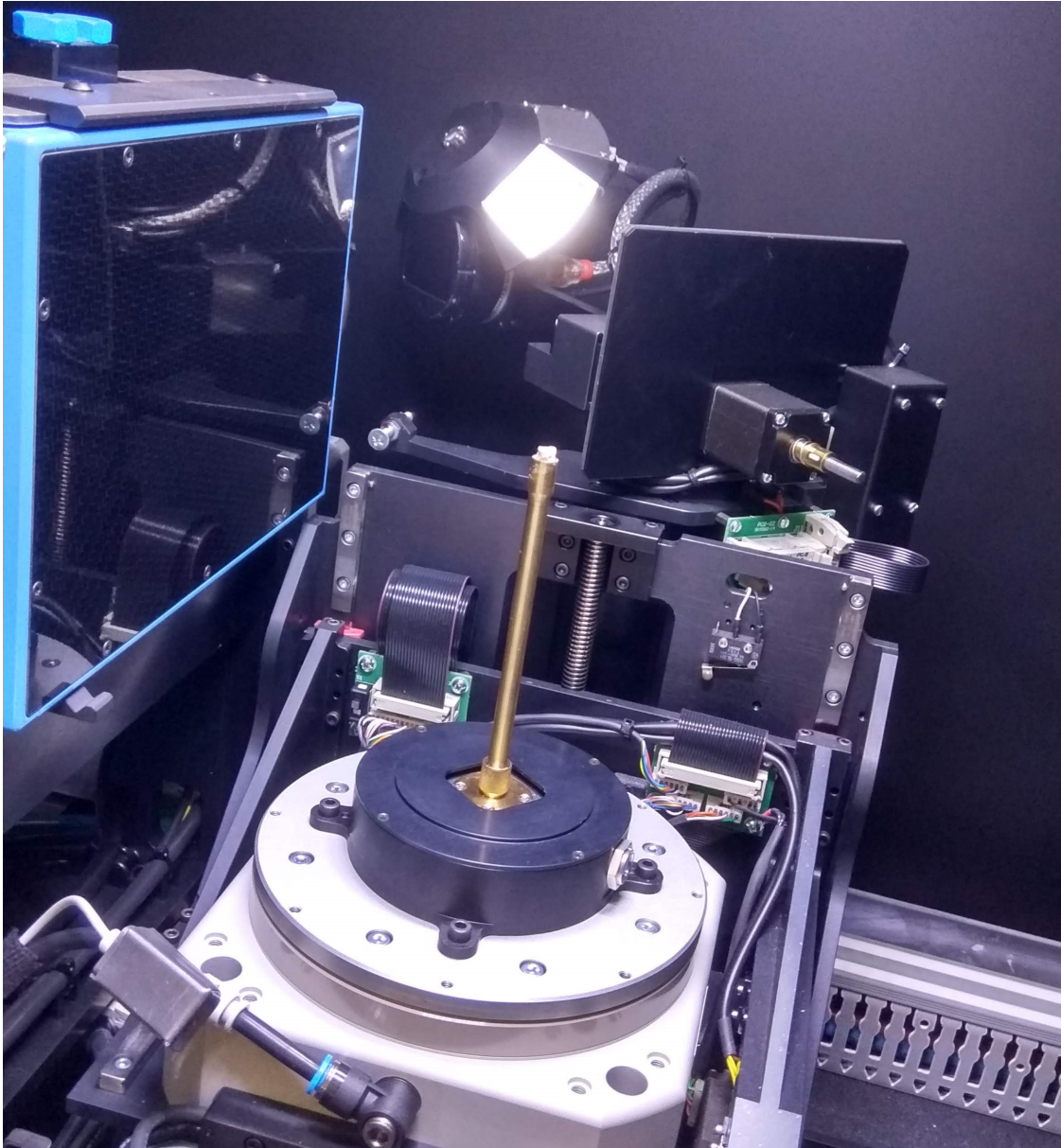


Figure 3.2: Picture of the sample chamber of the SkyScan 2211. At the center, in white, is the positioning system with a sample holder containing a sample 8 mm wide by 10 mm high. At the top-left corner, in blue, lies the flat panel. At the back, in black, and inclined, stays the cooled CCD camera behind a protective metallic plate. The source and filter mounting are to the right but are not accessible to take pictures.

Chapter 4

Experimental Part

4.1 Preparation method of the nanocomposite blocks to be used in the nanotomograph apparatus

In this section I will present the preparation method used for the creation of the nanocomposites studied in this work. The equipment in which the samples were measured highly influences the process of fabrication and it deserves to be shown and explained.

The preparation method is divided in two subsections: the mixture and the drying/moulding. The mixture section includes all the decisions taken regarding the type of solvent, amount and the steps for the mixing of the materials. The drying/moulding section will verse over what decisions were taken towards the production of samples usable for nanotomography analysis.

4.1.1 Mixture

The samples were mixed in a liquid environment using water as solvent. Since the samples would be dried afterwards the amount of water per samples was not critical factor. It was decided that, for 10g of clay, 8 ml of water was high enough to facilitate the mixing of the nanotubes with the clay and low enough so the drying time remains low. The mixture was done in a bowl using a hand held manual mixer. For the functionalized samples, 3 different weight percentages of nanotubes were used: 0.01 (1mg), 0.05 (5mg), 0.50 (50mg). The nanotubes were weighted

using an analytical scale with precision down to 0.1mg. The procedure was repeated to account for the kaolin and bentonite samples. Each batch of nanotubes was then dispersed in 8 ml of water using a 40w bath sonicator at a fixed frequency of 40kHz for 30 minutes. The CNTs were COOH-treated nanotubes so they are dispersible in water. After the sonication the CNT's dispersion was added to the 10 g of clay in a bowl and mixed with the hand held manual mixer for 5 minutes.

4.1.2 Drying and moulding

Samples for the nanotomograph have to be dry and have cylindrical symmetry as mentioned before in section 3.1. The first approach to obtain a cylindrical shape was using eppendorf vials (see Figure 4.1). The vials were 0.8 cm in diameter and 3.5 cm in depth. They also resisted temperatures of up to 120 degree Celsius. However, as wet clay occupies more volume than when dry, this meant that the clay would reduce in size as it dried inside the vial to the point where the sample would not end up being cylindrical. The first attempts using these vials resulted in oddly shaped flakes that were not appropriate to be used in the nanotomograph. The approach thus was changed to using out-of-the-shelf silicon cupcake-moulds. The mould tray consisted of 15 holes with a nearly cylindrical shape and a corrugated outer surface (See Figure 4.2 *a*). This time, instead of drying the samples into shape, the samples were dried in the moulds and then cut to remove the corrugated outer part and to reduce them in size (See Figure 4.2 *c*). The size of the moulds is 2.5 cm in diameter and 2 cm in depth. The samples once cut were 1cm in diameter and 1.5 cm in height (See Figure 4.2 *b*).

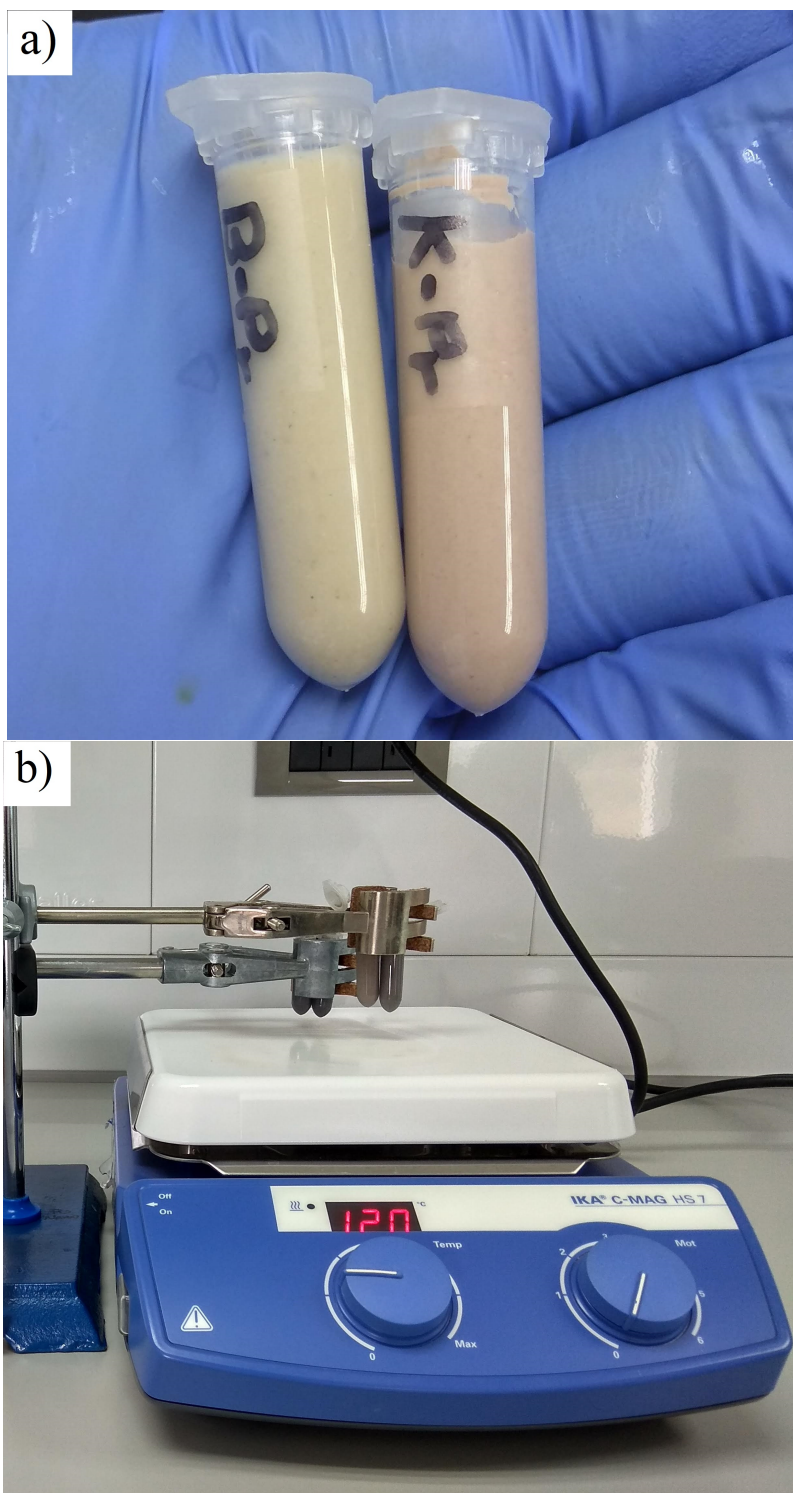


Figure 4.1: *a*), Eppendorf vials containing the control bentonite (B-Pr) and kaolinite (K-Pr) clays mixed with water. *b*), heating-plate at 120 degrees Celsius with four eppendorf vials drying on top.

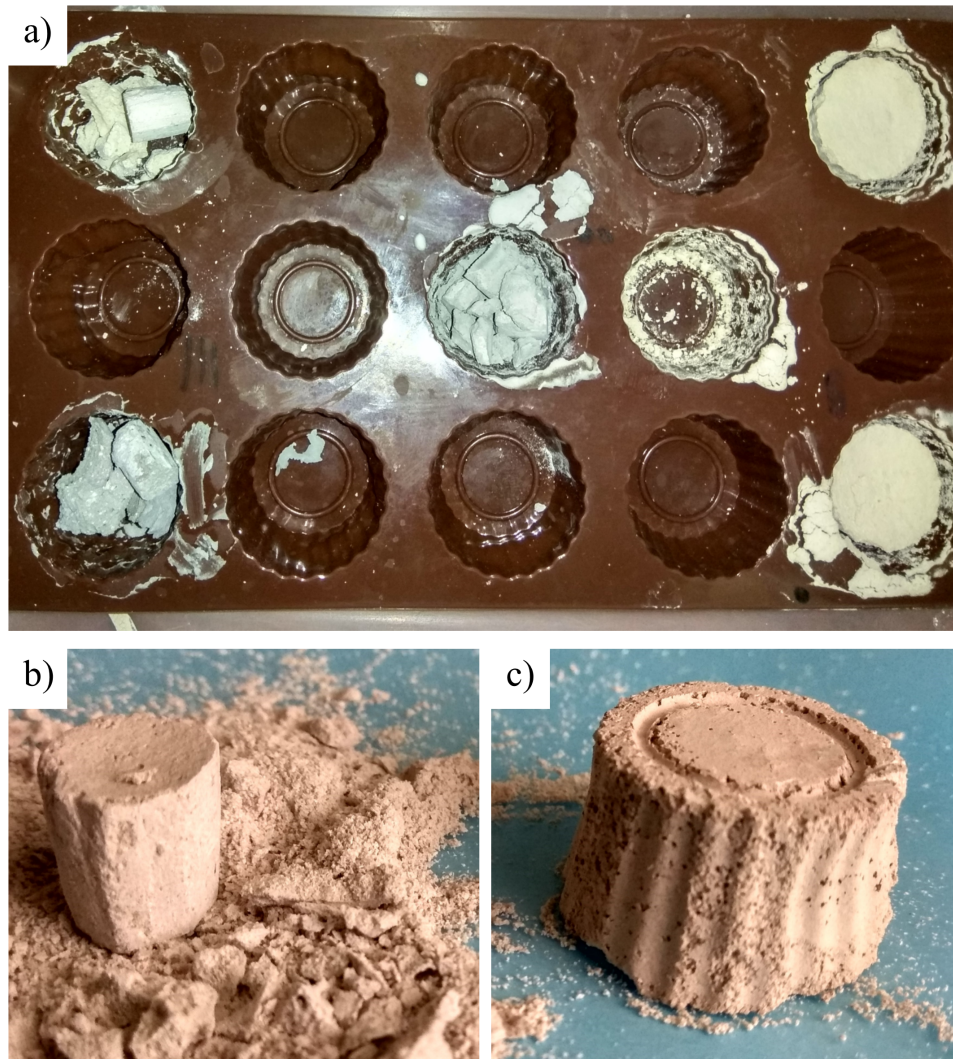


Figure 4.2: Pictures of the silicon mould and samples before and after being cut into shape. *a)*, the silicon mould used to dry the samples. It contains 5 samples: two of them are complete while the other 3 are already cut. The size of the mould is 2.5 cm in diameter and 2 cm in depth. *b)*, the kaolin pristine sample after being cut to reduce its size. *c)*, the kaolin pristine sample as it came out of the mould.

4.2 Reconstruction of the samples using BRUKER software

In this section I will explain the usage of the software provided by BRUKER. These software packages are provided with the CT equipment and are available for free download on their website.

4.2.1 NRecon software

The way the samples were placed inside the microCT apparatus and the measurement setup is detailed in the section 3.2. After the image acquisition was finished, the samples were reconstructed using the software provided alongside the microCT device. The process starts by executing GPUReconServer.exe. This program will manage the computation resources of the machine in order to optimize the reconstruction work. It detects the amount of CPUs available as well as the graphic cards (CUDA capable) and also the amount of memory available both for CPU and GPU computing. After that we can start the NRecon.exe software. At the start, a window will pop-up prompting us to import a data set (images obtained in the microCT device). After importing, some corrections have to be made to the data set before the reconstruction begins. On the right top panel, in the settings tab there are a number of features one can change to improve the quality of reconstruction (See Figure 4.3). Misalignment compensation helps to locate the centre of each picture at the centre of the object. Ring artifacts reduction helps to avoid the creation of rings in the reconstructed cylindrical object. These ring artifacts are caused by errors of the sensor during the image acquisition part of the measurement. Beam hardening and Smoothing are not used for this type of samples; we are looking for the porosity of the sample so the image should be as pristine and sharp as possible, these two settings may affect that. On one side, Beam hardening corrections are used to reduce the brightness of high attenuation objects in the scanned image and so may dissimulate impurities in the sample such as sand crystals or even metals. On the other hand, Smoothing makes an average of the color of surrounding pixel, this helps the image look less pixelated, but also causes a loss of information from those averaged pixels. There is no standard set of numbers applicable to all the samples. Each sample is different and the level of correction of each feature is different as well. After the tweaking of those settings we are ready to start reconstructing. We hit the start button in the start tab on the right panel and the program will start to write horizontal-section cuts of the 3d object to a subfolder inside the dataset folder. For the size of the samples in this work, the program will take between 14 and 20 min for each

reconstruction. The CUDA acceleration is crucial; without it, the time per reconstruction can be between 1h 40 m and 2 h. These horizontal-section cuts will then be used by the analysis softwares to obtain specific data from the sample.

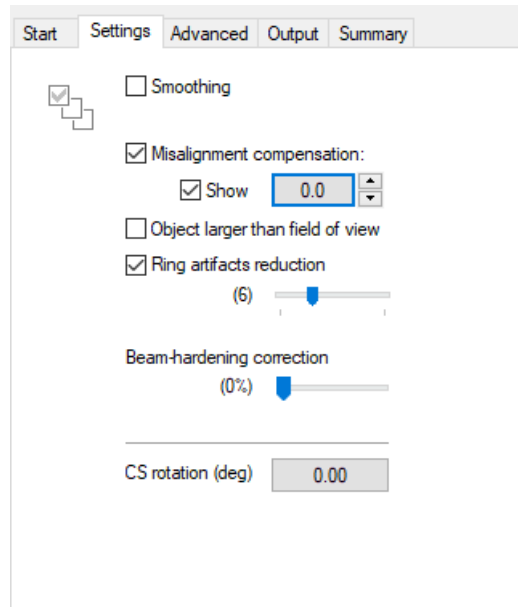


Figure 4.3: This image is a screenshot of the settings tab on the right side of the NRecon program. It shows the different corrections that can be made to the acquired images before doing the reconstruction; particularly, the value for ring artifacts correction and the value for missalignment compensation for the kaolin pristine sample.

4.2.2 CTvox Software

CTvox is another software that comes with the microCT device. It takes the section cuts created in the last step and creates a 3D map of the pixels in the 2D images.⁶⁴ In this software one can create images of the inside of the object or videos of the object. The first step is to open the CTvox.exe program. Once inside, go to the "Actions" tab and click "Load volume". A window will pop up and here select the pre-reconstructed data set. Only the first sectional cut needs to be selected as the program will import the rest following the same name. The images will load and

be stacked one over the next as to create a solid 3D object. This object can be rotated or moved inside the window. Next we need to identify our material. During the image acquisition section reflections over the surface of the sample create a kind of solid halo around the object. This has to be removed to see clearly just the object. This is done using the transfer function editor in the left panel in the window. It shows a graph where in the x-axis is the relative absorption of x-rays; and, in the y-axis is a measure of how visible areas with that specific absorption will be. Different materials need different transfer functions to become visible, so that one sample cannot be imaged using the same transfer function as another. To have a proper rendering one has to play with the lighting of the object, this is done clicking on the light bulb in the top bar. The same lighting protocol was used for both samples and is the same used for the samples in section 5.2. The objects were cut on one side to expose the interior and rotate 30 degrees horizontally and 20 degrees vertically to make the 3D structure more easy to visualize.

4.2.3 CTAn software

CTAn is a software provided by BRUKER for the analysis of the images generated on the reconstruction part of the process. It offers many features that include the generation of 3D models of specific parts of the object, e.g. open and closed pores. It also offers the ability to measure distances inside the object. Also, more important for this work, the program offers the feature of computationally measuring the amount and size of pores inside the sample and then calculate the porosity percentage⁶⁵. The process starts by loading the pre-reconstructed data-set to the program. Once loaded one has to select a type of region of interest (ROI). Only the material inside the region of interest will be analyzed. Due to the cylindrical shape of the samples, a round region of interest was used. The ROI was selected in a way that it excludes the outer perimeter of the sample. This was done primarily to avoid the counting of empty outer space as pore and second because the outside area was modified when the sample was cut into shape. After that, the next step is to select the pores inside the sample. The pores were selected as any material with x-ray absorbance index between 0 and 30. After that, a different number of plug-ins were applied to the object⁶⁵. After those steps, the outputs are a .csv file containing all the information about the porosity of the sample and 3 .ctm files containing 3D models of the open pores, the closed pores, and the separated solid material. These 3D files can be then uploaded to the CTVol program for visualization and rendering of images highlighting the different types of porosity.

The .csv file is used to plot the data of the porosity percentages for the different samples.

Chapter 5

Results & Discussion

In this chapter the nanotomograph reconstructed images and the porosity values of the samples are presented and discussed. First, the virtual reconstruction of the samples of pristine kaolin and bentonite clays are shown. These images are very important to understand the internal structure of the non-functionalized clay materials. They will also serve as comparison points to detect possible macroscopic changes inside the functionalized samples, e.g. fractures. Then, the 3D image reconstructions of the functionalized samples of kaolin and bentonite are shown. Here, a comparison is made between kaolin and bentonite samples with different content of CNTs. Third, the porosity values for the pristine samples of kaolin and bentonite are presented. Finally, the porosity values of the functionalized samples is shown making comparison within same clay samples and between the two type of clays.

5.1 3D reconstruction of the pristine Clay samples

The resulting images show both clay blocks in false-clay-like colouring (see Figure 5.1). In the kaolin sample (See Figure 5.1 *a*) a long microfracture is highlighted in the zoomed section. It possibly resulted from stress caused during drying. Pores are visible in both samples. The kaolin sample looks more compact and with fewer-118 compared 532- and smaller pores than the Bentonite sample (Figure 5.1, *b*). This can be attributed to the fact that kaolin does not swell too much when wet thus its inner structure does not contract too much during the drying process. On the other hand bentonite absorbs water when wet and it sips through the matrix and remains

there. When it dries, that water leaves spaces inside the matrix that can turn into pores (Refer to section 1.2.2). An example of this effect can be seen in the pore highlighted in Figure 5.1 *b*); it is a 2.5 mm by 1 mm hole inside the bentonite block that is larger than any pore in the Kaolin sample. In both samples we see some white-ish lumps with sizes ranging between 0.1 and 0.5 mm. These can be sections of the material that did not mix properly with water and remained the same during the whole process, or some high attenuation materials like crystals or metals introduced inside the matrix as contaminants.

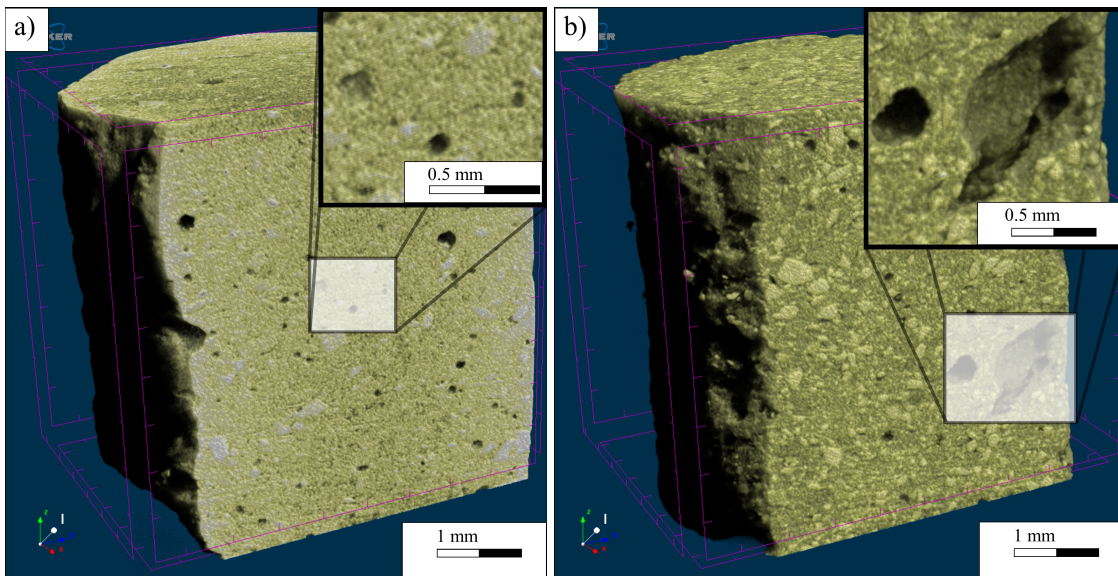


Figure 5.1: 3D reconstruction of the 2 pristine samples. *a*), kaolin clay; *b*), bentonite clay. The images show an inner cut of the samples where the pores as well as other internal structures, microfractures and contaminants, can be seen. The zoomed section of *a*) shows a microfracture around 1 mm long. The zoomed section in *b*) shows a big pore in the bentonite sample of around 2.5 mm by 1 mm. These images were produced completely using the CTvox software. The colour was tuned inside the program to resemble clay-like colour. A size mark of 1 mm and one of 0.5 mm in the zoomed section are included for reference.

5.2 3D reconstruction of CNT-Clay samples

For a more detailed description of the software used to create these images refer to section 4.2.2.

5.2.1 Kaoiln samples

The changes expected in the porosity are minimum and as such are not noticeable in the macroscopic images shown in this chapter. However, the images obtained in this part of the work help to recreate the samples and extract other qualitative data. Macroscopic pores are visible in all the three samples; 0.01 wt. %, 0.05 wt. %, and 0.50 wt. % (see Figure 5.2). Looking at the three samples in Figure 5.2 it appears that the amount of pores in *c* is greater than the amount of pores in *a*. This might be regarded to a wrong selection of parameters in the transfer function used in the render. An example of this is the fact that *b* looks darker as if it had more pores. This is countered by the porosity data presented in section 5.3. As it was mentioned before in Section 4.2.2, each sample has a different transfer function, then it becomes difficult to obtain specific data from this renders. The program CTvox is used only to highlight certain areas of the object for imagery. The appearance of some white-ish lumps can be seen as well in all three samples shown in Figure 5.2. These lumps also appeared in the pristine samples in figure 5.1 *a*. For that reason and the fact that no interaction between nanotubes and the Kaolin can result in such dense material, they are regarded as pre-existing features in the clay as grain impurities before the mixing .

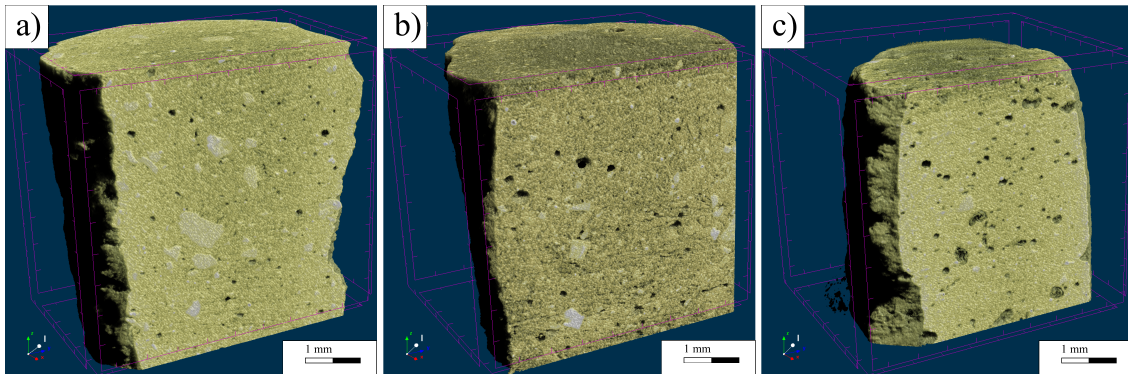


Figure 5.2: 3D reconstruction in false colour of the kaolin samples containing CNTs; *a*) 0.01 wt. %, *b*) 0.05 wt. %, *c*) and 0.50 wt. %. In the images are visible the internal structure of the nanocomposites. Different colours determine different densities here (See section 4.2.2). The

pores are also noticeable as shaded holes on the face of the blocks.

5.2.2 Bentonite samples

The bentonite samples in Figure 5.3 contain 0.01, 0.05, 0.5 % wt. of CNTs respectively. The evolution in the size and quantity of pores from *a* to *c* in Figure 5.3 shows also what appears to be an increase of porosity as the CNT content increases. However these images are just qualitative and the pore size as well as they are highly influenced by the right selection of transfer function prior rendering. The white lumps that appeared on the kaolin samples can be seen again in the three samples. However this time they are smaller, possibly because the material was sieved by the provider through a finer grid prior to being handed to me. The materials were not sieved once received from the providers. These renders offer great opportunities to study the macro-structure of materials like the ones inspected in this work. The ability to cut, highlight and reshape different part of the sample without destroying the original is highly appreciated for example in case were the material is expensive to recreate or the material is not physically present at all. It is one of the advantages provided by the nanotomography analysis. To extract specific data like, in our case, the porosity of the sample, it is necessary to use software designed for such purposes. In the following section the program CTAn will be used for that.

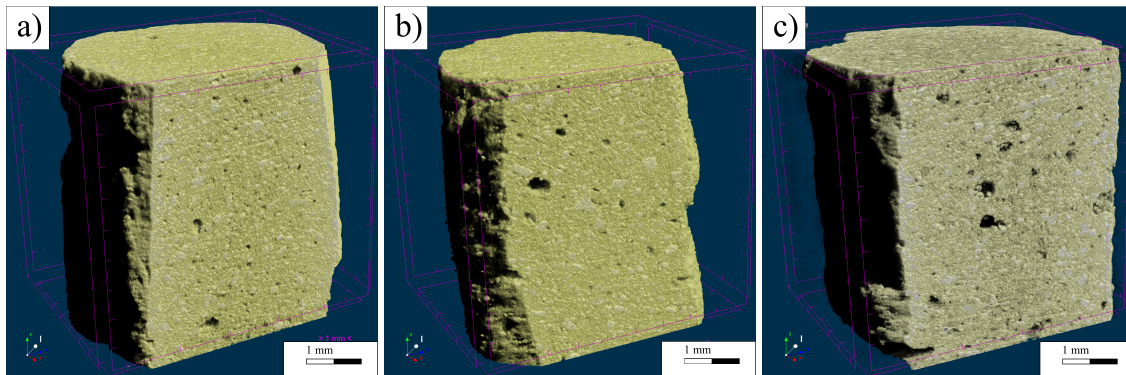


Figure 5.3: 3D reconstruction in false colour of the bentonite samples containing CNTs; *a*) 0.01 wt. %, *b*) 0.05 wt. %, *c*) and 0.50 wt. %. In the images are visible the internal structure of the nanocomposites. Different colours determine different densities here. The pores are also noticeable as shaded holes on the face of the blocks.

5.3 Porosity analysis of the Kaolin group of samples

In this section I will present and discuss the different values of porosity for the samples containing Kaolin. This group includes the pristine sample as it is key to determine whether or not and to which degree of extent does the CNT content affects the porosity in the material.

5.3.1 Plots of the porosity with respect to the CNT content

Figure 5.4 shows the plot of the open porosity for the 4 different kaolin samples: the pristine sample and the three that were added with CNTs. The vertical axis represents the porosity in %, and the horizontal axis represents the content of CNTs in wt.%.

Figure 5.4 corresponds to the plot of the total porosity of the sample. Here we can see adding 0.01 wt. % of CNTs decreases the porosity by more than 3%. The decrease continues onto the next concentration, 0.05 wt. %, although it is not as aggressive as the previous drop. The porosity % of the sample with the highest concentration of carbon nanotubes shows an increase to the point where it almost has the same porosity % as the pristine sample. While there is not enough plot points to establish a behaviour, it can be commented that there should be a value in between the third and fourth plotting points that minimises the porosity for the kaolin matrix. To try to explain this result better it is necessary to understand how the porosity is calculated. The porosity is calculated dividing the volume of empty space inside the sample by the sample's complete bulk volume. What we are measuring here is the volume of bubbles inside the matrix. What controls the volume of these bubbles is the surface tension of the material, a higher surface tension and the bubbles decrease in size and vice-versa for a lower surface tension. Carbon nanotubes, as seen in the first two functionalized samples, can help increase the surface tension and by doing so decrease the pore size inside the matrix. However, too high concentrations of nanotubes could have the inverse effect as the repulsion between them could decrease the surface tension and so result in higher pore sizes.

5.4 Porosity analysis of the bentonite group of samples

Figure 5.5 shows the variation in porosity of the bentonite matrix at different CNT concentration. The first thing that calls the attention in this plot is the drop of porosity between the pristine

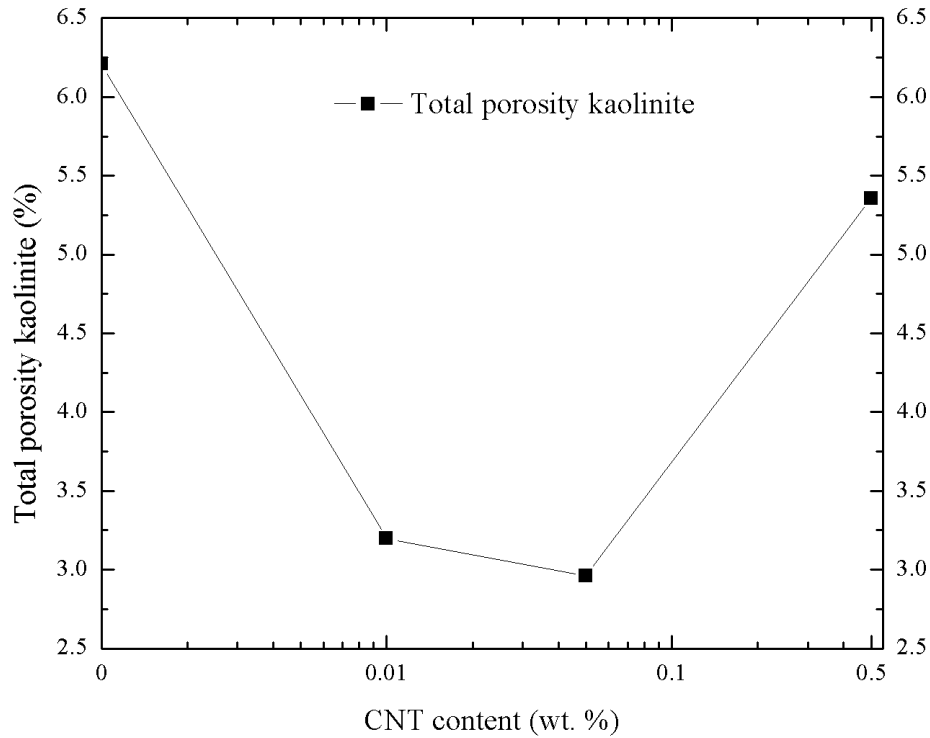


Figure 5.4: Plot of the porosity percentage with respect to the CNT content in wt. % for the Kaolin group of samples. The horizontal axis is in logarithmic scale.

sample and the one with 0.01 wt. % of CNT. The high porosity of the bentonite pristine sample is no surprise as the material is expected to swell when wet creating pores of very high size. The drop in the first two points of the plot is important because it means the nanotubes are acting against the normal swelling of the bentonite clay i.e. holding together the clay platelets avoiding separation. The next drop between the second and third sample is less aggressive than the first but still causes a decrease in porosity. The highest concentration has a higher porosity than the lowest non-zero concentration but still is more than 11 % below the value for the pristine sample. This means that even at high concentrations of nanotubes the porosity remains low. This contrasts

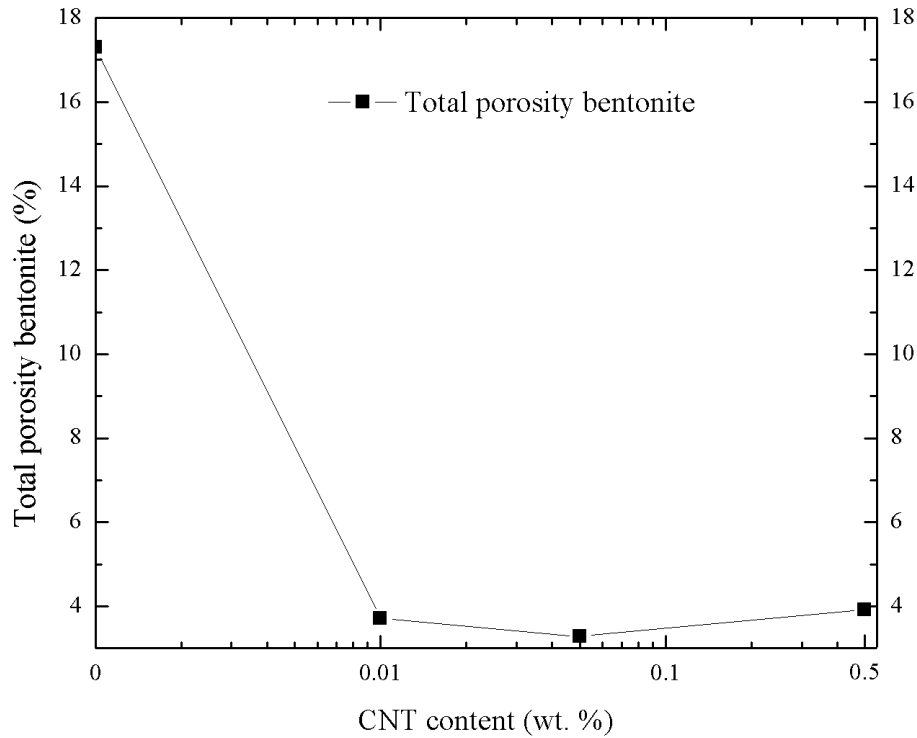


Figure 5.5: Plot of the porosity percentage with respect to the CNT content in wt. % for the Bentonite group of samples. The horizontal axis is in logarithmic scale.

with the kaolin group where the highest concentration of CNTs meant almost the same porosity as the pristine sample. This difference in the behaviour of both groups may lie in the structure of both clays. The main difference in their structure is that the kaolin clay shows a TO configuration and the bentonite shows a tri-layer TOT configuration. It can be presumed that the interaction of the nanotubes is stronger with the tetrahedral layer. That said CNTs will exert more pulling force between platelets in the bentonite than in the kaolin; resulting in a higher reduction of porosity in the bentonite than in the kaolin clay.

Chapter 6

Conclusions & Outlook

In this work I have studied the changes in porosity of two types of clay, bentonite and kaolin, when added with CNTs. Most of the focus of the work was in characterization as 3D x-ray nanotomography had seldom been used to characterize this type of samples and, as proven in this work, it can become a great tool for studying nano-modified materials. There was however some remarks on the fabrication method for these specific nanocomposites because of the restriction the technique imposes in the shape and state of the samples. The scans obtained from the two pristine samples show the different behavior of the two clays. It is visible in Figure 5.1 that Bentonite absorbs more water than kaolinite and thus is more porous when dried. Also, a comment about the plasticity of both clays can be done, as kaolinite showed cracks and fractures when dry, a feature that was absent from the bentonite sample even though it underwent a greater expansion as water evaporated from its matrix. The results obtained from modifying the kaolin were not as remarkable as those obtained in the bentonite sample. The drop in porosity was much more noticeable in bentonite and the increase caused by the highest concentration still was way below the pristine sample porosity. Overall it would seem that the TOT tri-layer configuration of bentonite makes it more suitable for controlling its porosity using additives as CNTs. Similar results were shown by Li *et al.*⁶⁶ for concrete added with CNTs where they found a decrease in pore size distribution and overall porosity of the concrete. The fact that different concentrations of CNTs can increase and decrease the pore size distribution inside clay matrices opens many possibilities in areas like construction⁶⁷ or the manufacture of filters⁶⁸. There are some limitations to the conclusions of this work. The first is the fact that only one type of CNTs (COOH-MWCNTs)

was used; perhaps other aspect ratios, chiralities or functional groups in the surface of CNTs may interact differently with the kaolin clay. Also, a more fine concentration grid should be used to create the samples and so have a more continuous plot from which better conclusion can be taken.

The advantages of using 3D x-ray nanotomography are palpable as it not only serves to the creation of virtual slices and 3D renders of the sample, but also can be used to retrieve important data of the sample as are connectivity and pore surface, volume and number. It has a great potential of becoming a tool for the characterization of nano-materials as it allows to look at the inside of the samples without destroying it as in other techniques. For this reason the methodology for its use in nanosciences should be scrutinized and improved continuously.

Appendix A

Complete Morphometry Results as extracted from the CTAn software.

In this appendix chapter I have included the morphometry results for all the samples. This data can be useful to reproduce my results and carry out other analysis using the raw porosity data, such as open porosity, closed porosity, pore surface, Euler number and connectivity. This values were not used for the present work because I wanted to study the specific changes of total porosity.

Description	Abbreviation	Value	Unit
Number of layers		889	
Lower vertical position		2700.00270000	um
Upper vertical position		10692.01069201	um
Pixel size		9.00000900	um
Lower grey threshold		20	
Upper grey threshold		255	
Total VOI volume	TV	123805947094.71985000	um ³
Object volume	Obj.V	116116579901.25496000	um ³
Percent object volume	Obj.V/TV	93.78917784	%
Total VOI surface	TS	148659203.18166688	um ²
Object surface	Obj.S	1101032444.40613320	um ²
Intersection surface	i.S	108145954.32588691	um ²
Object surface / volume ratio	Obj.S/Obj.V	0.00948213	1/um
Object surface density	Obj.S/TV	0.00889321	1/um
Centroid (x)	Crđ.X	-251.78147945	um
Centroid (y)	Crđ.Y	267.30296392	um
Centroid (z)	Crđ.Z	6709.69181639	um
Number of objects	Obj.N	118	
Number of closed pores	Po.N(cl)	431166	
Volume of closed pores	Po.V(cl)	4324993198.54032900	um ³
Surface of closed pores	Po.S(cl)	907484277.88893819	um ²
Closed porosity (percent)	Po(cl)	3.59094712	%
Volume of open pore space	Po.V(op)	3364373994.92456050	um ³
Open porosity (percent)	Po(op)	2.71745750	%
Total volume of pore space	Po.V(tot)	7689367193.46488950	um ³
Total porosity (percent)	Po(tot)	6.21082216	%
Euler number	Eu.N	394706	
Connectivity	Conn	36578	
Connectivity density	Conn.Dn	0.00000030	1/um ³

Table A.1: Morphometry Results of the pristine kaolin sample

Description	Abbreviation	Value	Unit
Number of layers		989	
Lower vertical position		1800.00180000	um
Upper vertical position		10692.01069201	um
Pixel size		9.00000900	um
Lower grey threshold		20	
Upper grey threshold		255	
Total VOI volume	TV	137732403924.04855000	um ³
Object volume	Obj.V	133329362846.18871000	um ³
Percent object volume	Obj.V/TV	96.80319159	%
Total VOI surface	TS	161908060.12525126	um ²
Object surface	Obj.S	305329936.35304594	um ²
Intersection surface	i.S	123675799.83220628	um ²
Object surface / volume ratio	Obj.S/Obj.V	0.00229004	1/um
Object surface density	Obj.S/TV	0.00221683	1/um
Centroid (x)	Crđ.X	-255.49761230	um
Centroid (y)	Crđ.Y	270.34918052	um
Centroid (z)	Crđ.Z	6245.93828587	um
Number of objects	Obj.N	201	
Number of closed pores	Po.N(cl)	51668	
Volume of closed pores	Po.V(cl)	1309632806.64440920	um ³
Surface of closed pores	Po.S(cl)	135913734.97174528	um ²
Closed porosity (percent)	Po(cl)	0.97269948	%
Volume of open pore space	Po.V(op)	3093408271.21543880	um ³
Open porosity (percent)	Po(op)	2.24595533	%
Total volume of pore space	Po.V(tot)	4403041077.85984800	um ³
Total porosity (percent)	Po(tot)	3.19680841	%
Euler number	Eu.N	49741	
Connectivity	Conn	2128	
Connectivity density	Conn.Dn	0.00000002	1/um ³

Table A.2: Morphometry Results of Kaolin + 0.01wt.% CNT:

Description	Abbreviation	Value	Unit
Number of layers		981	
Lower vertical position		1692.00169200	um
Upper vertical position		10512.01051201	um
Pixel size		9.00000900	um
Lower grey threshold		20	
Upper grey threshold		255	
Total VOI volume	TV	175594705875.09082000	um ³
Object volume	Obj.V	170395231599.82098000	um ³
Percent object volume	Obj.V/TV	97.03893449	%
Total VOI surface	TS	187061463.42884773	um ²
Object surface	Obj.S	450236420.21316952	um ²
Intersection surface	i.S	36574732.14942772	um ²
Object surface / volume ratio	Obj.S/Obj.V	0.00264231	1/um
Object surface density	Obj.S/TV	0.00256407	1/um
Centroid (x)	Crđ.X	-1.44832664	um
Centroid (y)	Crđ.Y	-0.43657786	um
Centroid (z)	Crđ.Z	6109.34539183	um
Number of objects	Obj.N	709	
Number of closed pores	Po.N(cl)	59413	
Volume of closed pores	Po.V(cl)	2324527486.68814090	um ³
Surface of closed pores	Po.S(cl)	239439920.56277281	um ²
Closed porosity (percent)	Po(cl)	1.34583762	%
Volume of open pore space	Po.V(op)	2874946788.58169560	um ³
Open porosity (percent)	Po(op)	1.63726279	%
Total volume of pore space	Po.V(tot)	5199474275.26983640	um ³
Total porosity (percent)	Po(tot)	2.96106551	%
Euler number	Eu.N	50228	
Connectivity	Conn	9894	
Connectivity density	Conn.Dn	0.00000006	1/um ³

Table A.3: Morphometry Results of Kaolin + 0.05wt.% CNT:

Description	Abbreviation	Value	Unit
Number of layers		812	
Lower vertical position		3393.00339300	um
Upper vertical position		10692.01069201	um
Pixel size		9.00000900	um
Lower grey threshold		20	
Upper grey threshold		255	
Total VOI volume	TV	113082575336.13676000	um ³
Object volume	Obj.V	107025218489.13437000	um ³
Percent object volume	Obj.V/TV	94.64342156	%
Total VOI surface	TS	138457583.33510694	um ²
Object surface	Obj.S	380831227.16076118	um ²
Intersection surface	i.S	104646349.99755286	um ²
Object surface / volume ratio	Obj.S/Obj.V	0.00355833	1/um
Object surface density	Obj.S/TV	0.00336773	1/um
Centroid (x)	Crđ.X	-251.20970566	um
Centroid (y)	Crđ.Y	270.27025989	um
Centroid (z)	Crđ.Z	7033.64991292	um
Number of objects	Obj.N	782	
Number of closed pores	Po.N(cl)	27762	
Volume of closed pores	Po.V(cl)	2784894706.66337590	um ³
Surface of closed pores	Po.S(cl)	200212589.17930382	um ²
Closed porosity (percent)	Po(cl)	2.53610039	%
Volume of open pore space	Po.V(op)	3272462140.33901980	um ³
Open porosity (percent)	Po(op)	2.89386948	%
Total volume of pore space	Po.V(tot)	6057356847.00239560	um ³
Total porosity (percent)	Po(tot)	5.35657844	%
Euler number	Eu.N	17116	
Connectivity	Conn	11428	
Connectivity density	Conn.Dn	0.00000010	1/um ³

Table A.4: Morphometry Results of Kaolin + 0.50wt.% CNT:

Description	Abbreviation	Value	Unit
Number of layers		1001	
Lower vertical position		1692.00169200	um
Upper vertical position		10692.01069201	um
Pixel size		9.00000900	um
Lower grey threshold		20	
Upper grey threshold		255	
Total VOI volume	TV	139403578743.56799000	um ³
Object volume	Obj.V	115283227432.98811000	um ³
Percent object volume	Obj.V/TV	82.69746621	%
Total VOI surface	TS	163497922.95848134	um ²
Object surface	Obj.S	3780578596.16333770	um ²
Intersection surface	i.S	93165281.17198046	um ²
Object surface / volume ratio	Obj.S/Obj.V	0.03279383	1/um
Object surface density	Obj.S/TV	0.02711967	1/um
Centroid (x)	Crđ.X	-290.92010308	um
Centroid (y)	Crđ.Y	290.72320712	um
Centroid (z)	Crđ.Z	6142.92766229	um
Number of objects	Obj.N	532	
Number of closed pores	Po.N(cl)	263234	
Volume of closed pores	Po.V(cl)	811776764.62730408	um ³
Surface of closed pores	Po.S(cl)	306856172.72332430	um ²
Closed porosity (percent)	Po(cl)	0.69923488	%
Volume of open pore space	Po.V(op)	23308574545.95257600	um ³
Open porosity (percent)	Po(op)	16.72021246	%
Total volume of pore space	Po.V(tot)	24120351310.57988000	um ³
Total porosity (percent)	Po(tot)	17.30253379	%
Euler number	Eu.N	-313562	
Connectivity	Conn	577328	
Connectivity density	Conn.Dn	0.00000414	1/um ³

Table A.5: Morphometry Results of Bentonite pristine:

Description	Abbreviation	Value	Unit
Number of layers		826	
Lower vertical position		2850.00427501	um
Upper vertical position		10687.51603127	um
Pixel size		9.50001425	um
Lower grey threshold		20	
Upper grey threshold		255	
Total VOI volume	TV	121409469879.37825000	um ³
Object volume	Obj.V	116909069586.83920000	um ³
Percent object volume	Obj.V/TV	96.29320489	%
Total VOI surface	TS	146403273.76979232	um ²
Object surface	Obj.S	304009339.20637679	um ²
Intersection surface	i.S	110784315.42541112	um ²
Object surface / volume ratio	Obj.S/Obj.V	0.00260039	1/um
Object surface density	Obj.S/TV	0.00250400	1/um
Centroid (x)	Crđ.X	-270.96592053	um
Centroid (y)	Crđ.Y	284.66106268	um
Centroid (z)	Crđ.Z	6772.67107527	um
Number of objects	Obj.N	565	
Number of closed pores	Po.N(cl)	31914	
Volume of closed pores	Po.V(cl)	1244073049.16909790	um ³
Surface of closed pores	Po.S(cl)	139689844.68449917	um ²
Closed porosity (percent)	Po(cl)	1.05293268	%
Volume of open pore space	Po.V(op)	3256327243.36994930	um ³
Open porosity (percent)	Po(op)	2.68210317	%
Total volume of pore space	Po.V(tot)	4500400292.53904720	um ³
Total porosity (percent)	Po(tot)	3.70679511	%
Euler number	Eu.N	25192	
Connectivity	Conn	7287	
Connectivity density	Conn.Dn	0.00000006	1/um ³

Table A.6: Morphometry Results of Bentonite + 0.01wt.% CNT:

Description	Abbreviation	Value	Unit
Number of layers		1001	
Lower vertical position		1692.00169200	um
Upper vertical position		10692.01069201	um
Pixel size		9.00000900	um
Lower grey threshold		20	
Upper grey threshold		255	
Total VOI volume	TV	139403578743.56799000	um ³
Object volume	Obj.V	134824878793.18185000	um ³
Percent object volume	Obj.V/TV	96.71550760	%
Total VOI surface	TS	163497922.95848131	um ²
Object surface	Obj.S	320387234.52609634	um ²
Intersection surface	i.S	123542279.85334544	um ²
Object surface / volume ratio	Obj.S/Obj.V	0.00237632	1/um
Object surface density	Obj.S/TV	0.00229827	1/um
Centroid (x)	Crđ.X	-262.17602720	um
Centroid (y)	Crđ.Y	270.37125844	um
Centroid (z)	Crđ.Z	6200.04798812	um
Number of objects	Obj.N	864	
Number of closed pores	Po.N(cl)	49162	
Volume of closed pores	Po.V(cl)	956647447.82705688	um ³
Surface of closed pores	Po.S(cl)	124792941.67088583	um ²
Closed porosity (percent)	Po(cl)	0.70454905	%
Volume of open pore space	Po.V(op)	3622052502.55908200	um ³
Open porosity (percent)	Po(op)	2.59824930	%
Total volume of pore space	Po.V(tot)	4578699950.38613890	um ³
Total porosity (percent)	Po(tot)	3.28449240	%
Euler number	Eu.N	34972	
Connectivity	Conn	15054	
Connectivity density	Conn.Dn	0.00000011	1/um ³

Table A.7: Morphometry Results of Bentonite + 0.05wt.% CNT:

Description	Abbreviation	Value	Unit
Number of layers		1001	
Lower vertical position		1692.00169200	um
Upper vertical position		10692.01069201	um
Pixel size		9.00000900	um
Lower grey threshold		20	
Upper grey threshold		255	
Total VOI volume	TV	139403578743.56799000	um ³
Object volume	Obj.V	133938035358.11682000	um ³
Percent object volume	Obj.V/TV	96.07933782	%
Total VOI surface	TS	163497922.95848134	um ²
Object surface	Obj.S	389147709.28997988	um ²
Intersection surface	i.S	124467415.06183982	um ²
Object surface / volume ratio	Obj.S/Obj.V	0.00290543	1/um
Object surface density	Obj.S/TV	0.00279152	1/um
Centroid (x)	Crđ.X	-270.48338709	um
Centroid (y)	Crđ.Y	272.52441346	um
Centroid (z)	Crđ.Z	6195.57144707	um
Number of objects	Obj.N	918	
Number of closed pores	Po.N(cl)	17246	
Volume of closed pores	Po.V(cl)	851194611.50587463	um ³
Surface of closed pores	Po.S(cl)	125446165.00161672	um ²
Closed porosity (percent)	Po(cl)	0.63150046	%
Volume of open pore space	Po.V(op)	4614348773.94529720	um ³
Open porosity (percent)	Po(op)	3.31006479	%
Total volume of pore space	Po.V(tot)	5465543385.45117190	um ³
Total porosity (percent)	Po(tot)	3.92066218	%
Euler number	Eu.N	-6282	
Connectivity	Conn	24446	
Connectivity density	Conn.Dn	0.00000018	1/um ³

Table A.8: Morphometry Results of Bentonite + 0.50wt.% CNT:

Bibliography

- [1] Kamigaito, O. What can be improved by nanometer composites? *Journal of the Japan Society of Powder and Powder Metallurgy* **1991**, 38, 315–321.
- [2] Camargo, P. H. C.; Satyanarayana, K. G.; Wypych, F. Nanocomposites: synthesis, structure, properties and new application opportunities. *Materials Research* **2009**, 12, 1–39.
- [3] Campillo, I.; Dolado, J.; Porro, A. High-performance nanostructured materials for construction. *Special Publication-Royal Society of Chemistry* **2004**, 292, 215–226.
- [4] Weaver, C. E. *Clays, muds, and shales*; Elsevier, 1989; Vol. 44.
- [5] Guggenheim, S.; Martin, R. Definition of clay and clay mineral: joint report of the AIPEA nomenclature and CMS nomenclature committees. *Clays and clay minerals* **1995**, 43, 255–256.
- [6] Bergaya, F.; Lagaly, G. *Handbook of clay science*; Newnes, 2013; Vol. 5.
- [7] Martin, R.; Bailey, S.; Eberl, D.; Fanning, D.; Guggenheim, S.; Kodama, H.; Pevear, D.; Srodon, J.; Wicks, F. Report of the clay minerals society nomenclature committee; revised classification of clay materials. *Clays and Clay Minerals* **1991**, 39, 333–335.
- [8] Schaller, C. Network Solids and Related Materials. <https://employees.csbsju.edu/cschaller/PrinciplesChem/network/NWalumina.htm>.
- [9] Beall, G. W. *Fundamentals of Polymer-Clay Nanocomposites*; Cambridge University Press, 2011.

- [10] Yu, M.-F.; Lourie, O.; Dyer, M. J.; Moloni, K.; Kelly, T. F.; Ruoff, R. S. Strength and breaking mechanism of multiwalled carbon nanotubes under tensile load. *Science* **2000**, *287*, 637–640.
- [11] Christidis, G. E. The concept of layer charge of smectites and its implications for important smectite-water properties. *EMU Notes Mineral* **2011**, *11*, 239–260.
- [12] Christidis, G. E.; Blum, A. E.; Eberl, D. Influence of layer charge and charge distribution of smectites on the flow behaviour and swelling of bentonites. *Applied Clay Science* **2006**, *34*, 125–138.
- [13] Christidis, G.; Eberl, D. Determination of layer-charge characteristics of smectites. *Clays and Clay Minerals* **2003**, *51*, 644–655.
- [14] Hammond, C. The elements. *Handbook of chemistry and physics* **2000**, *81*, 9.
- [15] Revankar, S. T. *Storage and Hybridization of Nuclear Energy*; Elsevier, 2019; pp 177–227.
- [16] Hirsch, A. The era of carbon allotropes. *Nature materials* **2010**, *9*, 868.
- [17] Grady, B. P. *Carbon nanotube-polymer composites: manufacture, properties, and applications*; John Wiley & Sons, 2011.
- [18] Dresselhaus, M. S.; Dresselhaus, G.; Eklund, P. C. *Science of fullerenes and carbon nanotubes: their properties and applications*; Elsevier, 1996.
- [19] Curl, R.; Kroto, H. W.; Smalley, R. E. Nobel prize in chemistry for 1996. *South African Journal of Chemistry-Suid-Afrikaanse Tydskrif Vir Chemie* **1997**, *50*, 102–5.
- [20] Tománek, D.; Enbody, R. J. *Science and application of nanotubes*; Springer Science & Business Media, 2000.
- [21] *Nanotubes and Related Nanostructures 2009: Volume 1204*; CAMBRIDGE UNIV PR, 2010.
- [22] Sanginario, A.; Miccoli, B.; Demarchi, D. Carbon nanotubes as an effective opportunity for cancer diagnosis and treatment. *Biosensors* **2017**, *7*, 9.

- [23] Yu, M.-F.; Kowalewski, T.; Ruoff, R. S. Investigation of the radial deformability of individual carbon nanotubes under controlled indentation force. *Physical Review Letters* **2000**, *85*, 1456.
- [24] Ruoff, R. S.; Tersoff, J.; Lorents, D. C.; Subramoney, S.; Chan, B. Radial deformation of carbon nanotubes by van der Waals forces. *Nature* **1993**, *364*, 514.
- [25] Javey, A.; Kong, J. *Carbon nanotube electronics*; Springer Science & Business Media, 2009.
- [26] Léonard, F. *Physics of carbon nanotube devices*; William Andrew, 2008.
- [27] Ouyang, M.; Huang, J.-L.; Cheung, C. L.; Lieber, C. M. Energy gaps in "metallic" single-walled carbon nanotubes. *Science* **2001**, *292*, 702–705.
- [28] Cundy, C. BKG Theng, Formation and Properties of Clay-Polymer Complexes. Elsevier Scientific Publishing Company, 1979. xii+ 362 pp. Price Dfl. 132. *Clay Minerals* **1980**, *15*, 99–99.
- [29] José-Yacamán, M.; Rendón, L.; Arenas, J.; Puche, M. C. S. Maya blue paint: an ancient nanostructured material. *Science* **1996**, *273*, 223–225.
- [30] Chung, D. D. *Composite materials: functional materials for modern technologies*; Springer Science & Business Media, 2013.
- [31] Parameswaranpillai, J.; Hameed, N.; Kurian, T.; Yu, Y. *Nanocomposite Materials: Synthesis, Properties and Applications*; CRC Press, 2016.
- [32] Yang, F.; Ou, Y.; Yu, Z. Polyamide 6/silica nanocomposites prepared by in situ polymerization. *Journal of Applied Polymer Science* **1998**, *69*, 355–361.
- [33] Alexandre, M.; Dubois, P. Polymer-layered silicate nanocomposites: preparation, properties and uses of a new class of materials. *Materials Science and Engineering: R: Reports* **2000**, *28*, 1–63.
- [34] Jannapu Reddy, R. Preparation, characterization and properties of injection molded graphene nanocomposites. Ph.D. thesis, Wichita State University, 2010.

- [35] Tanahashi, M. Development of fabrication methods of filler/polymer nanocomposites: With focus on simple melt-compounding-based approach without surface modification of nanofillers. *Materials* **2010**, *3*, 1593–1619.
- [36] Espinal, L. Porosity and its measurement. *Characterization of Materials* **2002**, 1–10.
- [37] Klobes, P.; Munro, R. G. *Porosity and specific surface area measurements for solid materials*; 2006.
- [38] Lowell, S.; Shields, J. E.; Thomas, M. A.; Thommes, M. *Characterization of porous solids and powders: surface area, pore size and density*; Springer Science & Business Media, 2012; Vol. 16.
- [39] Leofanti, G.; Padovan, M.; Tozzola, G.; Venturelli, B. Surface area and pore texture of catalysts. *Catalysis Today* **1998**, *41*, 207–219.
- [40] Herino, R.; Bomchil, G.; Barla, K.; Bertrand, C.; Ginoux, J. L. Porosity and pore size distributions of porous silicon layers. *Journal of the electrochemical society* **1987**, *134*, 1994–2000.
- [41] Kou, S.-C.; Poon, C.-S.; Etxeberria, M. Influence of recycled aggregates on long term mechanical properties and pore size distribution of concrete. *Cement and Concrete Composites* **2011**, *33*, 286–291.
- [42] Gesser, H.; Goswami, P. Aerogels and related porous materials. *Chemical Reviews* **1989**, *89*, 765–788.
- [43] Sepulveda, P.; Ortega, F.; Innocentini, M. D.; Pandolfelli, V. C. Properties of highly porous hydroxyapatite obtained by the gelcasting of foams. *Journal of the American Ceramic Society* **2000**, *83*, 3021–3024.
- [44] Sun, Z.; Lu, C.; Fan, J.; Yuan, F. Porous silica ceramics with closed-cell structure prepared by inactive hollow spheres for heat insulation. *Journal of Alloys and Compounds* **2016**, *662*, 157–164.

- [45] Abell, A.; Willis, K.; Lange, D. Mercury intrusion porosimetry and image analysis of cement-based materials. *Journal of colloid and interface science* **1999**, *211*, 39–44.
- [46] Kagan, D. N. *A-to-Z Guide to Thermodynamics, Heat and Mass Transfer, and Fluids Engineering*; Begellhouse.
- [47] Washburn, E. W.; Bunting, E. N. Porosity: VI. Determination of porosity by the method of gas expansion. *Journal of the American Ceramic Society* **1922**, *5*, 112–130.
- [48] Elliott, J. C.; Dover, S. X-ray microtomography. *Journal of microscopy* **1982**, *126*, 211–213.
- [49] Chen-Wiegart, Y.-c. K.; Wada, T.; Butakov, N.; Xiao, X.; De Carlo, F.; Kato, H.; Wang, J.; Dunand, D. C.; Maire, E. 3D morphological evolution of porous titanium by X-ray micro-and nano-tomography. *Journal of Materials Research* **2013**, *28*, 2444–2452.
- [50] Provis, J. L.; Rose, V.; Winarski, R. P.; van Deventer, J. S. Hard X-ray nanotomography of amorphous aluminosilicate cements. *Scripta Materialia* **2011**, *65*, 316–319.
- [51] others,, *et al.* Analysis of the three-dimensional microstructure of a solid-oxide fuel cell anode using nano X-ray tomography. *Journal of Power Sources* **2011**, *196*, 1915–1919.
- [52] Guizar-Sicairos, M.; Boon, J. J.; Mader, K.; Diaz, A.; Menzel, A.; Bunk, O. Quantitative interior x-ray nanotomography by a hybrid imaging technique. *Optica* **2015**, *2*, 259–266.
- [53] others,, *et al.* Hard X-ray Nanotomography of Catalytic Solids at Work. *Angewandte Chemie International Edition* **2012**, *51*, 11986–11990.
- [54] Attwood, D. Microscopy: Nanotomography comes of age. *Nature* **2006**, *442*, 642.
- [55] Tkachuk, A.; Duewer, F.; Cui, H.; Feser, M.; Wang, S.; Yun, W. X-ray computed tomography in Zernike phase contrast mode at 8 keV with 50-nm resolution using Cu rotating anode X-ray source. *Zeitschrift für Kristallographie-Crystalline Materials* **2007**, *222*, 650–655.
- [56] Withers, P. J. X-ray nanotomography. *Materials today* **2007**, *10*, 26–34.
- [57] Ostadi, H.; Rama, P.; Liu, Y.; Chen, R.; Zhang, X.; Jiang, K. Influence of threshold variation on determining the properties of a polymer electrolyte fuel cell gas diffusion layer in X-ray nano-tomography. *Chemical Engineering Science* **2010**, *65*, 2213–2217.

- [58] Peters, P. WC Roentgen and the discovery of x-rays. *Textbook of Radiology. Medcyclopedia.com, GE Healthcare* **1995**,
- [59] Seibert, J. A.; Boone, J. M. X-ray imaging physics for nuclear medicine technologists. Part 2: X-ray interactions and image formation. *Journal of nuclear medicine technology* **2005**, *33*, 3–18.
- [60] Macdonald, R. D. Design and implementation of a dual-energy X-ray imaging system for organic material detection in an airport security application. 2001.
- [61] Schreiner, M.; Frühmann, B.; Jembrih-Simbürger, D.; Linke, R. X-rays in art and archaeology: an overview. *Powder Diffraction* **2004**, *19*, 3–11.
- [62] Metcalfe, P.; Kron, T.; Hoban, P. *The physics of radiotherapy x-rays and electrons*; Medical Physics Publ., 2012.
- [63] Johansson, L. *Principles of Translational Science in Medicine*; Elsevier, 2015; pp 189–194.
- [64] Bruker, X-ray Micro-CT Microtomography. 2018; <https://www.bruker.com/products/microtomography/micro-ct-for-sample-scanning/x-ray-micro-ct-microtomography.html>.
- [65] 3D visualization of open and closed porosity. Bruker.
- [66] Li, G. Y.; Wang, P. M.; Zhao, X. Mechanical behavior and microstructure of cement composites incorporating surface-treated multi-walled carbon nanotubes. *Carbon* **2005**, *43*, 1239–1245.
- [67] Porter, J. F. Facing material with controlled porosity for construction boards. 2006; US Patent 7,049,251.
- [68] Yakub, I.; Du, J.; Soboyejo, W. Mechanical properties, modeling and design of porous clay ceramics. *Materials Science and Engineering: A* **2012**, *558*, 21–29.